Architecture-Engineered Electrospinning Cascade Regulates Spinal Microenvironment to Promote Nerve Regeneration

Yu Tang, Zonghan Xu, Jincheng Tang, Yichang Xu, Ziang Li, Wenbo Wang, Liang Wu, Kun Xi,* Yong Gu,* and Liang Chen*

The inflammatory cascade after spinal cord injury (SCI) causes necrotizing apoptosis of local stem cells, which limits nerve regeneration. Therefore, coordinating the inflammatory immune response and neural stem cell (NSC) functions is key to promoting the recovery of central nervous system function. In this study, a hydrogel "perfusion" system and electrospinning technology are integrated, and a "concrete" composite support for the repair of nerve injuries is built. The hydrogel's hydrophilic properties activate macrophage integrin receptors to mediate polarization into anti-inflammatory subtypes and cause a 10% increase in polarized M2 macrophages, thus reprogramming the SCI immune microenvironment. Programmed stromal cell-derived factor-1α and brain-derived neurotrophic factor released from the composite increase recruitment and neuronal differentiation of NSCs by approximately four- and twofold, respectively. The fiber system regulates the SCI immune inflammatory microenvironment, recruits endogenous NSCs, promotes local blood vessel germination and maturation, and improves nerve function recovery in a rat SCI model. In conclusion, the engineering fiber composite improves the local inflammatory response. It promotes nerve regeneration through a hydrophilic programmed cytokine-delivery system, which further improves and supplements the immune response mechanism regulated by the inherent properties of the biomaterial. The new fiber composite may serve as a new treatment approach for SCI.

1. Introduction

The expansion of the global construction and transportation industries has led to an annual increase in the incidence and mortality rates of spinal cord injuries (SCIs), making this a public health concern.[1] After an injury, nerves have the potential to regenerate; however, in cases of severe inflammation, there is often a risk of repair failure.[2] While mechanophysical injuries after primary SCI lead to neuronal and axonal death, subsequent activation of innate immune responses amplifies the extent of primary injury and lesion.[3] Therefore, in recent years, research on SCI treatment has focused on regulating the inflammatory response in the acute phase, improving the microenvironment of the SCI, and providing a suitable foundation for the proliferation and differentiation of endogenous neural stem cells (NSCs).[4] However, the cascade effect of malignant inflammation in the local area of the injury restricts the recruitment of NSCs; this prevents the formation of a bridging network, resulting in low neural repair efficiency.[5] Therefore, understanding how to regulate the local immune microenvironment and promote the migration and differentiation of endogenous stem cells into neuronal cells is the key to breaking through the bottleneck of treating SCIs.

In the acute stage of SCI, the permeability of the blood-spinal cord barrier is enhanced. The activation of the innate immune response recruits neutrophils, monocytes, dendritic cells, and macrophages to the injury site, with blood-borne mononuclear and microglia macrophage activation peaking 3 and 7 days after injury because of damaged local chemotaxis. Macrophages can be polarized into classically activated macrophages (M1) and alternatively activated macrophages (M2), the latter type involved in inflammatory reactions.[6] In the acute SCI stage, M1 macrophages remove tissue debris and promote neovascularization and antigen presentation. However, the imbalanced local microenvironment leads to excessive polarization of M1, resulting in severe inflammatory reactions and disturbance of M1/M2 spontaneous conversion ability. Studies have shown that the dynamic balance between M1 and M2 subtypes provides a favorable microenvironment for the neuronal differentiation of NSCs, which determines the prognosis of SCI.[7] After SCI, endogenous NSCs migrate to the site of injury, where they proliferate and differentiate into different functional types of cells such as neurons, oligodendrocytes, and astrocytes. Although

Y. Tang, Z. Xu, J. Tang, Y. Xu, Z. Li, W. Wang, L. Wu, K. Xi, Y. Gu, L. Chen
Department of Orthopedics
the First Affiliated Hospital of Soochow University
Orthopedic Institute
Soochow University
188 Shizi Road, Suzhou, Jiangsu 215006, P. R. China
E-mail: xikun@suda.edu.cn; guyong1019@suda.edu.cn; chenliang7737@suda.edu.cn

the immune inflammatory microenvironment at the site of injury can be partially improved, the number of migrated NSCs is hindered by the lack of neurotrophic factors for survival, proliferation, and neurogenic differentiation.[8]

Various biological materials have been developed for nerve repair strategies, with different topologies, intrinsic compositions, and electromagnetic abilities.[9] These materials exhibit specific effects on the immunomodulatory and inflammatory microenvironment and endogenous NSCs.[10] However, because of the complex biological environment of SCI, the characterization of materials alone cannot accurately and sequentially balance the host's inflammatory response and local nerve regeneration.[11] Therefore, it is feasible to introduce suitable biological factors and further modify the biological materials to achieve the precise programmed release of loaded biological factors for precisely regulating the inflammatory immune microenvironment and directing endogenous NSC migration and differentiation.

We previously developed the L-polylactic acid (PLLA) microsol (MS) electrospinning technology to generate multifunctional biomaterials for therapeutic applications. Some characteristics of this system are simple preparation technique; the arrangement of a natural neural extracellular matrix orientation via fiber simulation; contact guide neurites and axon growth; as high as 80% load cell factor of drug-loading rate; slow-release time throughout 6 weeks; and blocking of the local malignant microenvironment to avoid recruitment of harmful biological factors. PLLA is an excellent carrier for delivering nerve differentiation signals and support and guidance to nerve regeneration.[12] However, natural nerve fibers are highly hydrophilic; thus, the hydrophobic nature of PLLA may limit the biological effects of the provided cells. To improve the surface hydrophilicity of the material, the PLLA surface needs to be modified. Hydrogels have good hydrophilicity, which in addition to maintaining the physiological function of cells, regulates macrophage inflammation.[13] Methylacrylylated gelatin (GelMA) hydrogel provides a new strategy for modifying PLLA scaffolds; GelMA contains RGD and MMP sequences, has an affinity for cell surface integrin receptors, and influences cell effects through the "outside–inside" biological information transmission mode of the membrane.[14] Studies have shown that this pattern can promote the expression of anti-inflammatory subtypes in macrophages, but the specific mechanism remains unclear. Thus, modification of the PLLA surface with GelMA not only improves its hydrophilicity but may also enable the regulation of macrophage polarization to control inflammation levels. After SCI, primary mechanical and secondary responses at the injury site lead to necrosis of NSCs in situ and the absence of signals for the recruitment of systemic stem cells.[15]

Artificially supplementing neurotrophic factors and providing biological signals have become viable methods for regulating NSCs.[16] Brain-derived neurotrophic factor (BDNF) is a widely expressed protein in the central nervous system with neurotrophic effects. BDNF promotes nerve cell survival and increases synaptic plasticity and neurogenesis.[17] Stromal cell-derived factor-1α (SDF-1α) plays a role in nerve repair through the SDF-1α/CXC chemokine receptor pathway and chemotactic stem cell migration to the injury site following a concentration gradient.[18]

This study was based on the characteristics of a healthy central nervous extracellular matrix and an acute SCI microenviron-ment pathological feature of inflammation that led to a lack of endogenous NSCs. The architectural reinforced concrete structure inspired the model: we aimed to build immunomodulatory and nerve repair functions on biomimetic scaffolds to sustain the inhibition of acute inflammation triggered by SCI and meet tissue regeneration requirements. Using amide linkage water gel-coating microsol electrospinning technology, the GelMA hydrogel was rendered with high hydrophilicity, swelling properties, and SDF-1α release characteristics. This structure induced macrophages and microglia to polarize toward M2 and secrete anti-inflammatory factors, causing a reduction in local inflammation of SCIs and encouraging the germination of blood vessels. Rapid regulation of acute immune inflammation and improvement of NSC homing provided a good environment for subsequent nerve repair. Furthermore, the core–shell structure of the electrospun fiber continuously released BDNF, which promoted the neuronal differentiation of NSCs and achieved neural function recovery. We also investigated the structural properties of the biomimetic composite fibers, the loading efficiency of SDF-1α and BDNF, and the regulation of biological effects on macrophages and NSCs in vitro. The combined effect of hyper-hydrophilic regulation of the immune response and programmed release of SDF-1α and BDNF to promote neural function recovery of the composite fibers was verified in an SCI rat model in vivo. These results demonstrate that the composite fibers may represent an attractive novel anti-inflammatory and repair treatment approach for SCI.

2. Results and Discussion

2.1. Overview of the Fiber Scaffold Groups

A schematic diagram of the structure design and synthesis of the microsol-electrospun GelMA hydrogel scaffold is shown in **Scheme 1**. In this study, we generated four fiber scaffolds described in Experimental Section: PLA scaffolds, PLLA fibers produced by electrospinning technology; MS, PLLA electrospinning with the core–shell structure containing BDNF; MS@G, MS coated with GelMA; and MS@G/S, MS coated with GelMA loaded with SDF-1α. The details are shown in **Table 1**.

2.2. Production of the Directional MS Electrospun Scaffold with GelMA Coating Technology

Considering the directional fiber structure and mechanical properties of the spinal cord, an engineered nerve graft should ideally be composed of oriented fibers that are soft, tightly connected to the nerve stump, resistant to deformation during movement, and loaded with relevant cytokines, drugs, and/or seed cells.[19] Electrospinning technology has been used to develop fiber scaffolds for SCI,[20] and PLLA and hyaluronic acid (HA) are widely used in regenerative tissue engineering.[21] We loaded a stable microsol PLLA spinning solution containing BDNF into a syringe. Under a strong electric field, the solution formed Taylor cones at the syringe tip. Next, we collected the oriented nanoscale fiber filaments through parallel shock rods.

GelMA is a double-bond modified gelatin with unique properties compared with natural materials. In addition to its use in 3D
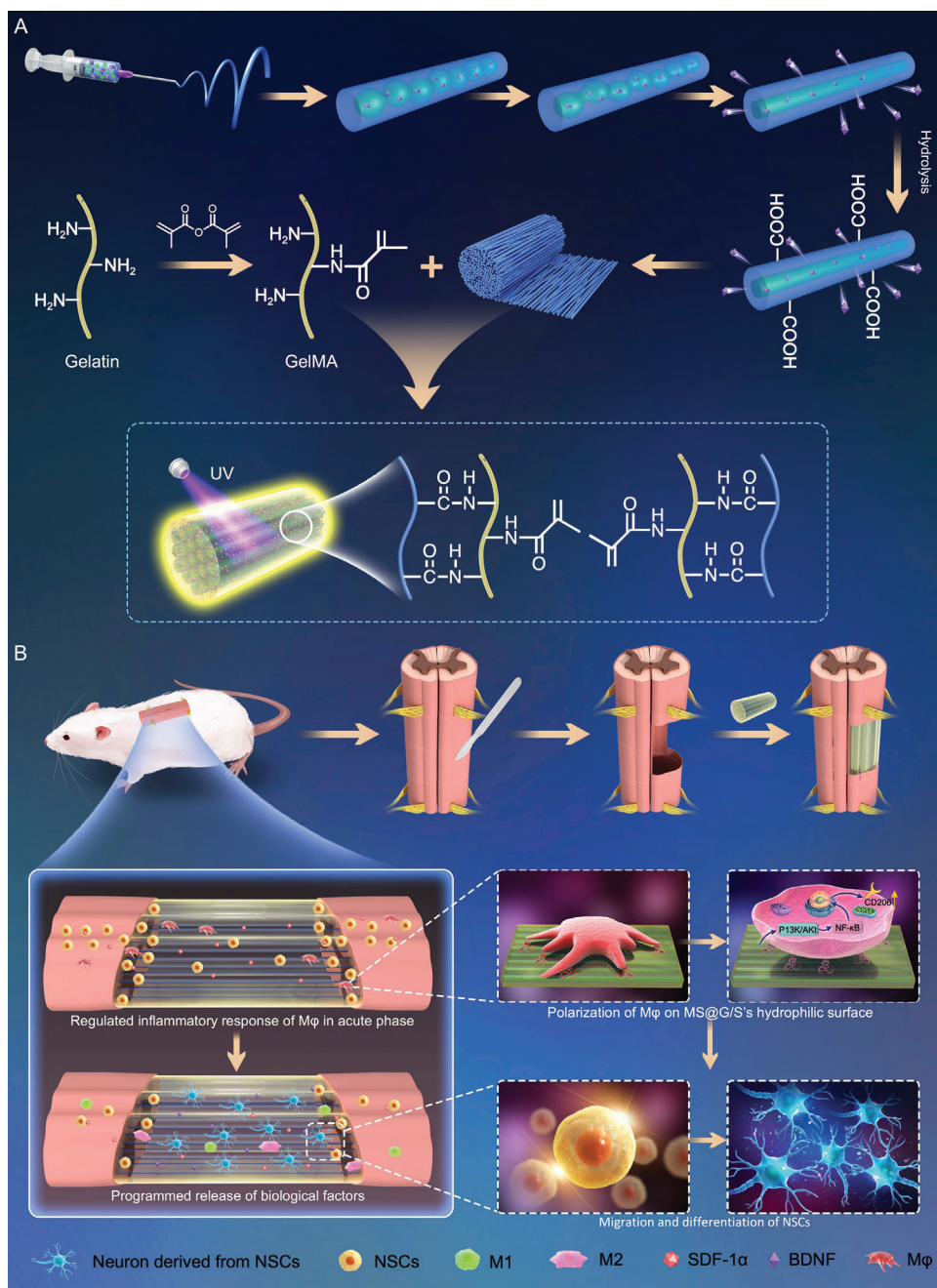
Scheme 1. Structure and effect mechanism of composite fiber. A) Scheme illustration of the construction of MS@G/S. B) Its role in microenvironment-responsive immune regulation and nerve regeneration.

Table 1. Fiber scaffolds.

Grouping	Abbreviation	Function
PLLA electrospinning	PLA	Control group
PLLA electrospinning with core–shell structure containing BDNF	MS	Control group
MS coated with GelMA	MS@G	Control group
MS coated with GelMA/SDF-1α	MS@G/S	Experimental group

cell culture, tissue engineering, biological 3D printing, and other applications, GelMA is frequently applied in medical and clinical fields.[22] GelMA coating technology was used to make GelMA solution, evenly loaded with cytokines, form amide bonds through the −COOH reaction generated by partial hydrolysis of −NH2 and MS. The solution was used to coat the fiber surface evenly.[23] The final scaffold was formed after photo-crosslinking.

Scanning electron microscopy (SEM) was used to observe the morphology of the fiber scaffolds. The results showed that the fiber distribution was more regular and oriented after acquiring
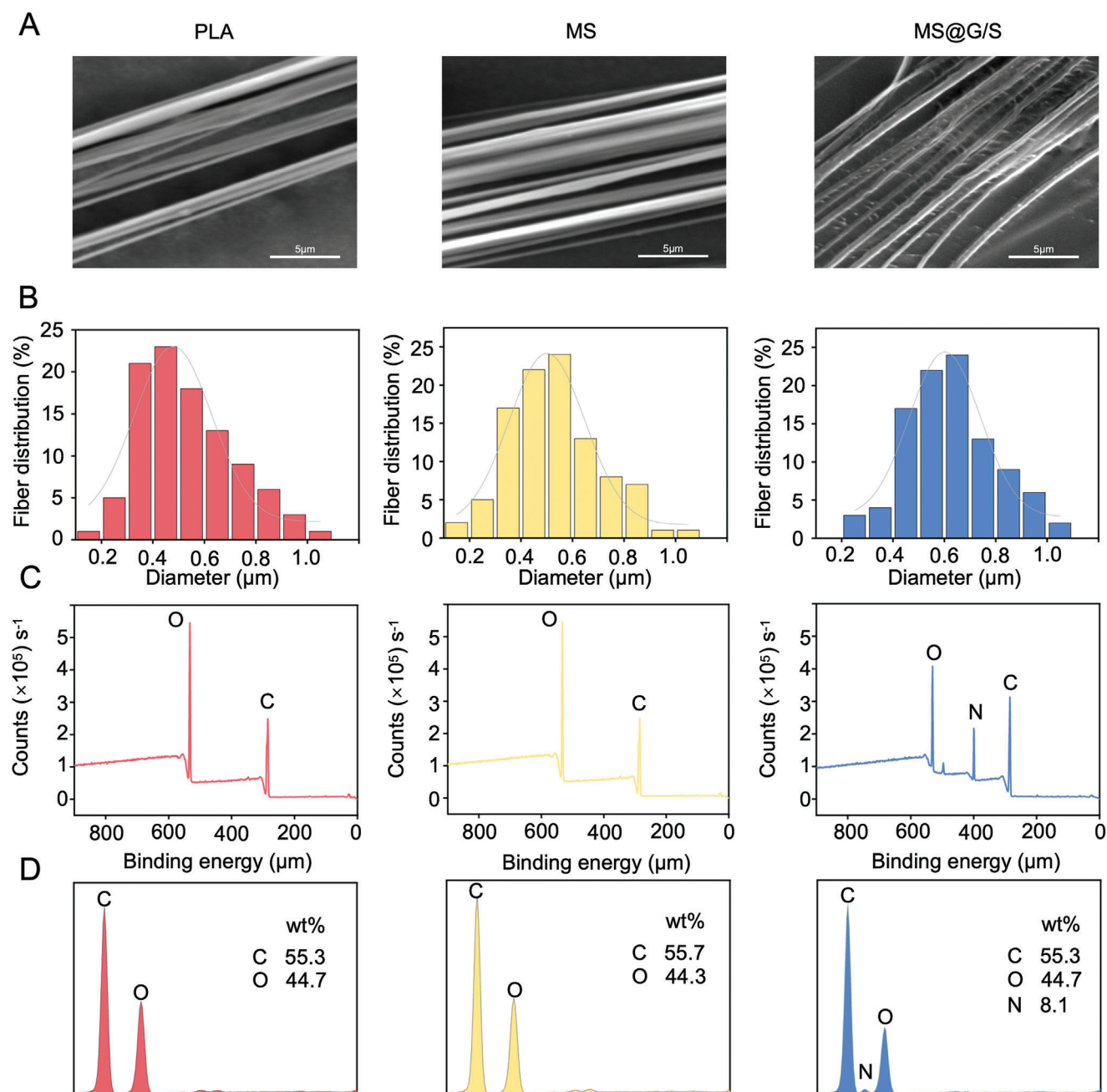
**ADVANCED
SCIENCE NEWS**

www.advancedsciencenews.com

**ADVANCED
HEALTHCARE
MATERIALS**

www.advhealthmat.de

Figure 1. Morphology of different fiber scaffolds. A) SEM images of different fiber scaffolds. B) Histogram of the frequency distribution of different fiber stent diameters (*n* = 100). C) XPS indicating chemical elements on the surface of different fiber scaffolds. D) EDS indicating chemical elements and proportion of different fiber scaffolds.

a parallel electrode receiver (**Figure 1**A). The clear GelMA coating could be captured on the MS@G/S surface. To evaluate the size and uniformity of the electrospun fibers, 100 fibers were randomly selected from the SEM images, and the distribution of fiber diameters was examined (Figure 1B). The diameters of the PLA, MS, and MS@G/S fibers were 0.557 ± 0.16, 0.531 ± 0.17, and 0.628 ± 0.17 μm, respectively.

Directionally spun fibers can function as templates for tissue regeneration and reserve layers for the programmed re-

lease of nerve growth factors. The core–shell structure formed in microsol-electrospun fibers determines the controlled release ability and directly affects the regeneration effect of scaffolds. One of the conditions for constructing a core–shell structure is that HA microsol is uniformly distributed in methylene chloride (DCM). We next used the dynamic light scattering (DLS) method to determine the particle size and distribution. The average size of the microsol particles was 311 nm, and the polydispersity index (PDI) was 0.208, indicating that the particle distribution was
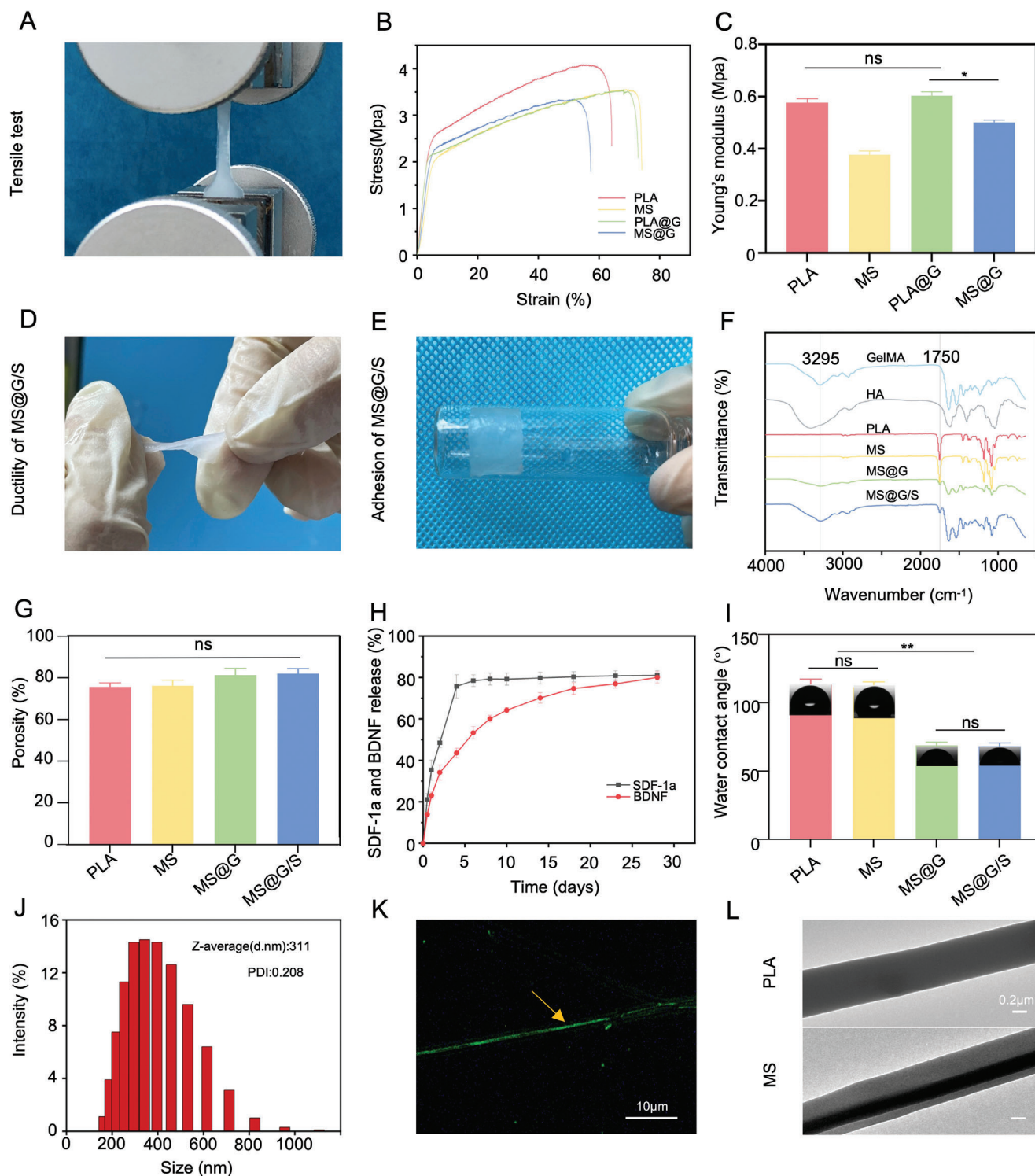
Figure 2. Physical and chemical properties of nanofiber scaffolds. A–C) Schematic diagram and results of the mechanical tensile test and Young's modulus of different fiber scaffolds. D,E) Good ductility and adhesion of MS@G/S in wet conditions. F) FTIR spectra of different fiber scaffolds. G) Porosity of different fiber scaffolds. H) Release curves of SDF-1α and BDNF in MS@G/S. I) The water contact angles of different fiber scaffolds were evaluated. J) Particle size analysis: distribution of HA micro sol particle diameter in DCM. K) Distribution of FITC-BSA in fiber scaffolds. L) TEM images of PLA and MS (all values were mean ± std. dev., statistical analysis evaluated by one-way analysis of variance (ANOVA) with Tukey's post-hoc test; $n = 3$, ns, not statistically significant; *$p < 0.05$, **$p < 0.01$).

**ADVANCED
SCIENCE NEWS**

www.advancedsciencenews.com

**ADVANCED
HEALTHCARE
MATERIALS**

www.advhealthmat.de

uniform (**Figure 2**J). To visualize the internal structure of the microsol fibers, transmission electron microscopy (TEM) was used. While a bare fiber structure was observed in the PLA group, the typical core–shell structure was confirmed in the MS group (Figure 2L).

The successful construction of the core–shell structure and the effective grafting of GelMA can also be demonstrated by examining the surface elemental composition of fiber scaffolds. Three analyses were performed to measure each fiber scaffold's surface chemical elements. X-ray photoelectron spectroscopy (XPS) was first conducted and revealed no significant differences in the carbon (C 285.7 eV) and oxygen (O 536.8 eV) peaks on PLA and MS fiber surfaces (Figure 1C), indicating that HA microsol particles were located inside the fibers. However, the carbon and oxygen peaks increased significantly, and a nitrogen (N 406.8 eV) peak appeared, indicating the presence of grafted GelMA on the fiber surfaces. EDS was performed (Figure 1D). The wt% of C and O in the PLA groups were 55.3% and 44.7%, respectively, and the wt% of C and O in the MS groups were 55.7% and 44.3%; in the MS@G group, wt% of C, N, and O were 55.3%, 44.7%, and 8.1%, respectively. To verify the success of grafting, Fourier transform infrared spectroscopy (FTIR) was performed to evaluate the chemical bonds and functional group structure on the fibers (Figure 2F). The results showed no significant difference between the infrared spectra of PLA and MS groups. Thus, the absence of a HA characteristic band in MS. During the spinning process, all the microsol particles are encapsulated in the fiber's core. The GelMA fiber contains $-NH_2$, and a band of $-NH_2$ was observed at 3295 cm^{-1}, the same peak as the amide bond produced by the reaction, but no C=O band at 1750 cm^{-1} was detected. The MS@G and MS@G/S fibers showed a distinct pattern of C=O bands at 1750 cm^{-1}, indicating the successful grafting of GelMA to the surface of MS fiber scaffolds.

After SCI, the spinal cord is unstable, especially at the damaged stump junction. A neural tissue engineering graft with good mechanical strength and adhesion ability is a suitable connection device for the spinal cord stump. In addition, it improves the stability of the spinal cord. Figure 2A–C shows that MS@G/S exhibited good tensile properties under wet conditions. The stress–strain curves showed that the electrospun fibers with PLLA as raw material had considerable tensile strength. In the MS group, the HA core–shell structure sacrificed tensile strength to a certain extent, with Young's modulus being 0.380 ± 0.015 MPa. However, in the MS@G/S group, the GelMA coating led to a slightly lower maximum tensile strength than the PLA fiber and Young's modulus of 0.50 ± 0.010 MPa. These results indicated that the GelMA coating compensated for the decrease in the maximum tensile strength caused by the HA core–shell structure, which may be from the amide bond interactions between GelMA and fibers, which led to a partial fusion between hydrophobic and hydrophilic materials, resulting in improvement of the overall strength of the material. Figure 2D,E shows the good plasticity of MS@G/S and adhesion to smooth glass slides under compression conditions. The promising result was the lasting bond formed. Together, these results show that the MS@G/S scaffold had strong resilience and good bonding ability, ensuring continuous close contact with the injured end of the spinal cord under physiological conditions and during exercise.

Hydrophobicity/hydrophilicity influences the biocompatibility of materials, which plays an important role in tissue engineering.[24] Therefore, we measured the water contact angles of the different fiber scaffolds. The contact angles of PLA, MS, MS@G, and MS@G/S fibers were 113.13 ± 4.16°, 111.43 ± 3.90°, 86.87 ± 2.37°, and 68.13 ± 2.45°, respectively (Figure 2I). No significant differences were observed in the contact angle between the PLA and MS groups, which is likely because while the MS fibers have an internal core–shell structure, its outer layer is the same as that of PLA. The other two groups with GelMA coating (MS@G and MS@G/S) had significantly lower water contact angles than the PLA and MS groups ($p < 0.01$). These results showed that GelMA coating significantly improved the hydrophilicity of the fiber scaffold surface, which made up for the disadvantages caused by the hydrophobicity of PLLA.

As one of the three essential elements of tissue engineering, seed cells play a more significant role with more sufficient growth space. Electrospun scaffolds satisfy this condition, providing a spatial location for cells to grow.[25] Our results showed that the diameter of the fiber scaffolds in the MS@G/S group was slightly larger than that in the PLA and MS groups; additionally, there was no statistically significant difference in porosity (Figure 2G). This phenomenon may also be explained by the GelMA coating. During the grafting process, GelMA crowds the space between adjacent fibers; however, because of the porous shape of GelMA, the internal bulk density does not increase too much, resulting in an insignificant change in porosity.

2.3. Spatial and Temporal Release of Coagulated Fiber Scaffolds

In addition to terrain guidance, the biological or chemical characteristics of the fiber scaffold generate a permissive microenvironment for recruited NSCs to function effectively. Temporal and spatial factors play key roles in regulating neural repair and stem cell regulation. Recent studies have found that rat NSCs emerge after 1 day of SCI and peak at 5 days; however, the differentiation of the recruited NSCs often takes several months for motor behavior recovery.[26] Therefore, there is an urgent need to establish spatiotemporal drug delivery systems carrying multiple drugs/bioactive molecules to accurately regulate stem cell migration and differentiation. In this study, to obtain the sequential release of SDF-1α and BDNF, BDNF was coated on the core–shell structure of the HA particle comprised of nanofibers and SDF-1α was combined with the GelMA hydrogel and grafted onto the surface of the nanofibers. Figure 2K shows the distribution of BNDF wrapped in HA particles after electrospinning. The distribution of fluorescently labeled BSA was relatively uniform and stable and was present in each electrospun fiber, which laid the foundation for the sustained release of drugs in vivo. The release of SDF-1α and BDNF in vitro was detected using an enzyme-linked immunosorbent assay (ELISA).

As shown in Figure 2H, there was an early release of SDF-1α in the first few days, during which approximately 75.72 ± 2.77% of SDF-1α was released; the release rate gradually slowed down, and on the 14th day, it was ≈79.73 ± 2.85% of the initial load. The release of BDNF exceeded 81.04 ± 2.30% of the initial loaded volume in the MS@G/S group. However, the overall BDNF release was continuous and slow, and the release rate gradually slowed

**ADVANCED
SCIENCE NEWS**

www.advancedsciencenews.com

**ADVANCED
HEALTHCARE
MATERIALS**

www.advhealthmat.de

down. The total release amount was 70.12 ± 2.52% on day 14, and the final release was completed at 28 days; the total drug release amount exceeded the initial drug-loading amount by 80.02 ± 2.73%. These results suggested that functionalized fiber hydrogels provide a rapid initial release of SDF-1α followed by a sustained release of BDNF. The orderly release of both may play a precise role in regulating stem cell migration and differentiation, which is critical in SCI recovery. This process is analogous to watering and fertilizing seeds at specific times to encourage germination and growth. Notably, the regeneration of specific tissues, including the spinal cord and bone, requires precise regulation of the repair process.[27] Overall, our results showed the successful construction of MS@G/S for the sequential release of biological factors.

2.4. Biocompatibility and Adhesion

As a template for cell adhesion and proliferation, fiber membranes are required to have good cell compatibility. Thus, we next seeded BMSCs on different fibrous membranes and examined survival and proliferation. After 3 days of culture, cells were stained, and live and dead cells were counted in three different fields (Figure S1A,B, Supporting Information). Reflecting the poor biocompatibility of pure PLA fiber membranes, the number of living cells growing in the PLA group was significantly less than that of the MA@G/S group ($p < 0.05$). No differences were observed in the MS group (prepared by HA and BDNF by microsol electrospinning) and the pure PLA group; this may be because HA is inside the MS group's fibers and does not improve the hydrophobicity of PLLA. The GelMA-coated groups (MS@G and MS@G/S) showed no significant difference in live/dead cell numbers compared with the control group (on a 24-pore plate).

To further compare the biocompatibility of the materials, BMSCs were inoculated on different fiber scaffolds. After 1, 3, 5, and 7 days of culture, the proliferation of BMSCs was detected by the CCK-8 method (Figure S1C, Supporting Information). The results showed that BMSCs proliferated and grew on the surface of all materials, and the number of cells in each group showed an upward trend from day 1 to day 7. In general, the cells in the control group (on cell culture plates) proliferated better than cells on all the fiber scaffolds. However, significantly more cells were detected on the fiber membranes coated with GelMA (MS@G and MS@G/S groups) than with the simple polymer fiber membrane (PLA and MS groups).

Immunofluorescence labeling of integrin expression in BMSC membranes showed that cells cultured on GelMA-coated fiber membranes expressed higher integrin levels than those cultured on PLA or MS fiber membranes alone (Figure S2A, Supporting Information). This indicates a significant promotion of integrin β1 subunit expression by the GelMA coating. While no significant differences in integrin expression were detected between the PLA group and MS group, the fluorescence signal of the two groups was lower than that of the control group ($p < 0.05$). This may be because the dishes of the cells cultured with the fiber scaffolds were treated with a vacuum plasma, allowing the cells to adhere more efficiently, and providing better biomechanical stress to the cells. BMSCs cultured on MS@G/S for 3 days were well spread and tightly adhered to the material, as observed by TEM (Figure S2B, Supporting Information). Semi-quantification of the integrin immunostaining was consistent with the images (Figure S2C, Supporting Information). The directional structure of the fibrous membranes also induces BMSCs to move in the specified direction. These results show that the GelMA coating mimics ECM and provides a suitable environment for cell adhesion and proliferation.

2.5. Establishment of NSCs and NSCs Migration

After SCI, NSCs respond to specific signals, become activated, and migrate to the damaged area. At the injury site, NSCs proliferate and undergo differentiation into multiple cell types, including astrocytes, oligodendrocytes, neurons, and other cells, to participate in reconstructing neural circuits. The number of endogenous NSCs is limited and peaks at 5–7 days after injury. At the injury site, NSCs migrate to either end of the lesion and are frequently unable to transverse the entire lesion and/or reach the other end.[28] How to promote the recruitment of NSCs to both sides of the nerve stump is a current focus in SCI research. Using endogenous NSCs avoids the ethical and physiological problems associated with foreign stem cell transplantation. We thus next evaluated the influence of the fibers on NSC migration in vitro using Transwell chamber experiments. NSCs were extracted from fetal rat brains and confirmed by Nestin expression (**Figure 3**A,B). NSCs were planted in the top chamber, and the composite fibers were placed in the bottom chamber. The SDF-1α cytokine alone was used as a positive control.

A schematic diagram of the assay is shown in Figure 3C. We found NSCs in the top compartment of chambers containing MS@G/S or SDF-1α solution showed increased cell migration compared with PLA, MS, and MS@G, indicating recruitment by SDF-1α. We also observed that the migrating NSCs accumulated into neurospheres, indicating that the migrated NSCs exhibited division and proliferation abilities. Quantification of the migration data confirmed that SDF-1α effectively recruited NSCs; the number of migrated NSCs in the MS@G/S group was approximately fourfold higher than controls (Figure 3D). These results also indicated that MS@G/S fibers rapidly release GelMA-loaded SDF-1α in a short period.

2.6. Macrophage Phenotype and Integrin Activation

From a philosophical point of view, the essence of neural regeneration involves the response of various cells to the SCI microenvironmental signals, similar to the relationship between human development and society.[29] In this study, we focused on the relationship between fiber scaffolds, Mφ, HUVECs, and NSCs and the interaction mechanism from the aspects of the immune microenvironment, angiogenesis, and subsequent neurogenic differentiation.

The regulation of macrophages in the neuroimmune microenvironment initiates tissue repair. Therefore, we next investigated the direct interactions between the fiber scaffolds and Mφ and the influence on Mφ phenotypes.

Proinflammatory M1Mφ tends to express high levels of CD86 and secrete inflammation-related biomolecules, such as TNF-α,
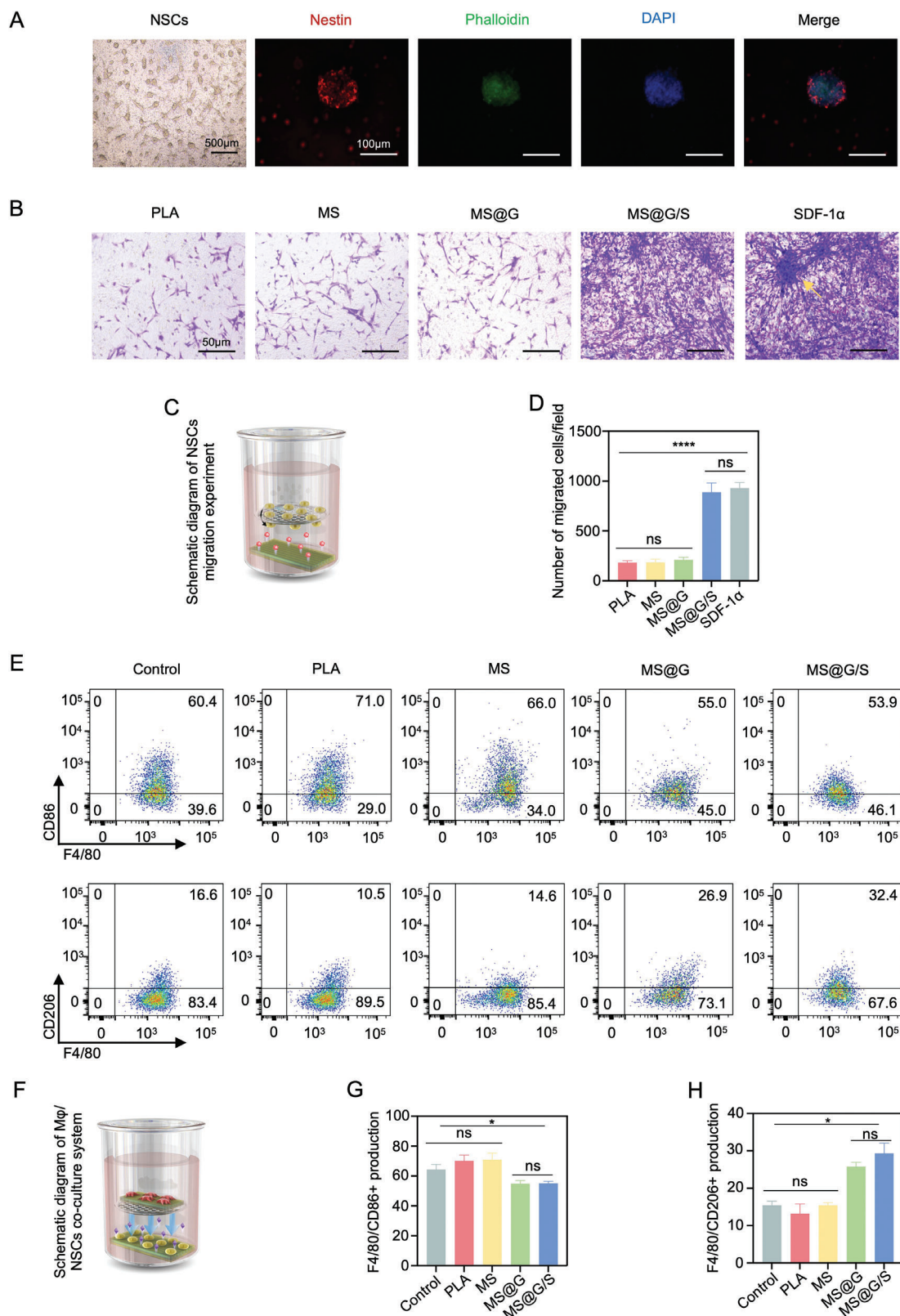
Figure 3. A) Culture of NSCs and immunofluorescence staining of characteristic surface markers. B,D) NSCs migration experiment and quantitative analysis of the number of migrating cells. C,F) Schematic diagram of NSCs migration test and Mφ/NSCs co-culture system. E) Expression of CD86 and CD206 on Mφ at 7 days by flow cytometry. G,H) Quantitative analysis of FCA at 7 days (all values were mean ± std. dev., statistical analysis evaluated by one-way analysis of variance (ANOVA) with Tukey's post-hoc test; $n = 3$, ns, not statistically significant; $*p < 0.05$, $****p < 0.0001$).

INOS, IL-1β, and IL-6, while M2Mφ highly express CD206 and shows reduced levels of inflammation-related biomolecules such as IL-10 and IL-4. M1Mφ and M2Mφ are in a dynamic equilibrium state and jointly regulate the microenvironment of SCI. To investigate the interactions of fiber scaffolds, Mφ, and NSCs, we used a Transwell co-culture system; Mφ and the fiber membrane was cultured in the top chamber, and NSCs and the fiber membrane were cultured in the bottom chamber (Figure 3F). After 7 days, flow cytometry analysis was used to identify the polarization phenotype of Mφ in the top chamber (Figure 3E,G,H). The proportions of M1 in the PLA and MS groups (without GelMA coating) were $70.10 \pm 4.41\%$ and $70.93 \pm 4.41\%$, respectively, and the proportions of M2 were $13.16 \pm 2.65\%$ and $15.40 \pm 0.72\%$. In the GelMA-coated groups (MS@G and MS@G/S), the proportions of M1 were $54.87 \pm 2.10\%$ and $55.10 \pm 1.37\%$, and the proportions of M2 were $25.77 \pm 1.15\%$ and $29.37 \pm 2.68\%$, respectively. Significantly, more F4/80/CD206 double-positive cells were observed in the GelMA-coated groups (MS@G, MS@G/S) than in the PLA and MS groups.

Immunofluorescence staining was performed to further investigate differences in Mφ polarization; F4/80 was used to label Mφ, INOS was used to label the M1 subtype, and CD206 was used to label the M2 subtype (**Figure 4**A,C). In the PLA group and MS group, INOS signal intensity was higher than the CD206 signal, while in the MS@G group and MS@G/S group (with GelMA coating), a stronger CD206 signal was observed compared with the INOS signal; there was no statistical difference between the two groups (Figure 4B,D).

To further evaluate the influence of GelMA on the immunoregulation of macrophages, macrophages were co-cultured with different fiber scaffolds for 7 days, and the expression of M1 genes, M2 genes, proinflammatory genes, and anti-inflammatory genes were detected by qRT-PCR (Figure 4E–J). CD206 and Arginase-1 gene expressions were higher in the MS@G/S group than in the PLA and MS groups, indicating that GelMA coating promoted the polarization of BMM to M2. In addition, the expressions of proinflammatory genes IL-1β and TNF-α in the MS@G/S group were also lower than those in the control group, while the expression of IL-10 was significantly higher ($p < 0.01$). This suggested that GelMA coating exhibited immunomodulatory function, promoting the polarization of M2 macrophages and exerting an inhibitory effect on inflammation. This may be because the GelMA coating improves the hydrophilicity of the fiber scaffolds, which may result in better cell adhesion.

Previous studies have shown that hydrophilicity may be related to various signaling pathways regulating macrophage polarization, including the SrC-ROCK, Wnt, NF-κB, and PI3K/Akt pathways.[30] The integrin receptor is expressed in macrophage adhesion and modulates downstream signaling pathways including IRF5, JAK/STAT, NF-κB, and PI3K/Akt pathways.[31] We speculated that the induction of macrophage polarization by the improved hydrophilicity of biomaterials might be related to the P13K/Akt signaling pathway mediated by integrins, so we selected this pathway for further analysis.

Interactions between the ECM and the cell affect the cellular phenotype. Integrins are common transmembrane protein receptors ubiquitous on the surface of vertebrate cells and play a key role in signal transduction between the ECM and the cytoskeleton. To explore the molecular mechanisms by which the gel coat-

ing stimulates macrophage polarization, we performed a western blot analysis of proteins related to the integrin β1/PI3K/AKT signaling pathway. The results showed that the relative expressions of integrin β1, p-Akt/AKT, and p-PI3K/PI3K significantly increased. In contrast, the expression of NF-κB decreased in the MS@G and MS@G/S groups compared with the PLA and MS groups (without GelMA coating) (**Figure 5**A–G). This indicated that PI3K/AKT signaling was activated. We speculate that activated PI3K inhibited NF-κB activation through the Akt signaling pathway, and NF-κB induced the M1 phenotype of macrophages. We found that macrophages differ in their ability to adhere to hydrophilic/hydrophobic scaffolds, thereby influencing the expression of integrins. Increased integrin may activate the downstream PI3K/AKT signaling pathway, up-regulate the expression of M2 phenotypic genes CD206, IL-10, and Arg-1, and promote M2 polarization. These results were consistent with the results reported by Mettouchi et al., showing that integrin β1 was associated with PI3K/Akt activation.[32]

Taken together, these results suggested that alterations in integrin expression induced by hydrophilic biomaterials on fiber scaffolds may be associated with characteristic alterations in cellular activity. In addition, the balance of M1Mφ and M2Mφ was tilted toward M2 in the presence of GelMA-coated scaffolds, which led to a change of subsequent signals, constituting the start switch for reprogramming the immune microenvironment for tissue repair. At the same time, it provided better conditions for angiogenesis and neuronal regeneration in the injured region.

2.7. Mφ Promotes HUVEC Tube Formation through Paracrine Effects

Studies have shown that the germination and maturation of blood vessels in tissues cannot be separated from the involvement of macrophages, and the degree of vascularization affects the prognosis of tissue repair.[33] We detected vascular endothelial growth factor (VEGF) and platelet-derived growth factor-BB (PDGF-BB), two major cytokines involved in the recruitment, growth, and maturation of vascular endothelial cells, in Mφ co-cultured with different fiber membranes by ELISA (Figure 5I). We further explored the effects of Mφ/fiber scaffolds on angiogenesis using HUVEC tube formation assays. The supernatant from the Mφ/fiber membrane co-culture was collected and mixed with endothelial cell medium at a ratio of 1:1 for use in HUVEC culture. As shown in Figure 5H, after 3 and 6 h of HUVEC culture in supernatant from the MS@G and MS@G/S groups, abundant vascular-like reticular structures were observed, while only a few tubular structures were observed in the PLA and MS groups. The number of tubular nodes and the length of tubular structures were measured (Figure 5J,K). The average tube length of the MS@G/S group at 3 and 6 h of culture was 5755 ± 345 and 7645 ± 253 μm, respectively; no statistical difference was detected compared with the MS@G group. In the PLA group, the lengths at 3 and 6 h were 3953 ± 298 and 5569 ± 131 μm, respectively, and significant differences were observed compared with the MS@G/S group. The trend of the average number of nodes was consistent with the trend of the tube length. Compared with the PLA and MS groups, the MS@G and MS@G/S groups showed better vascular formation ability
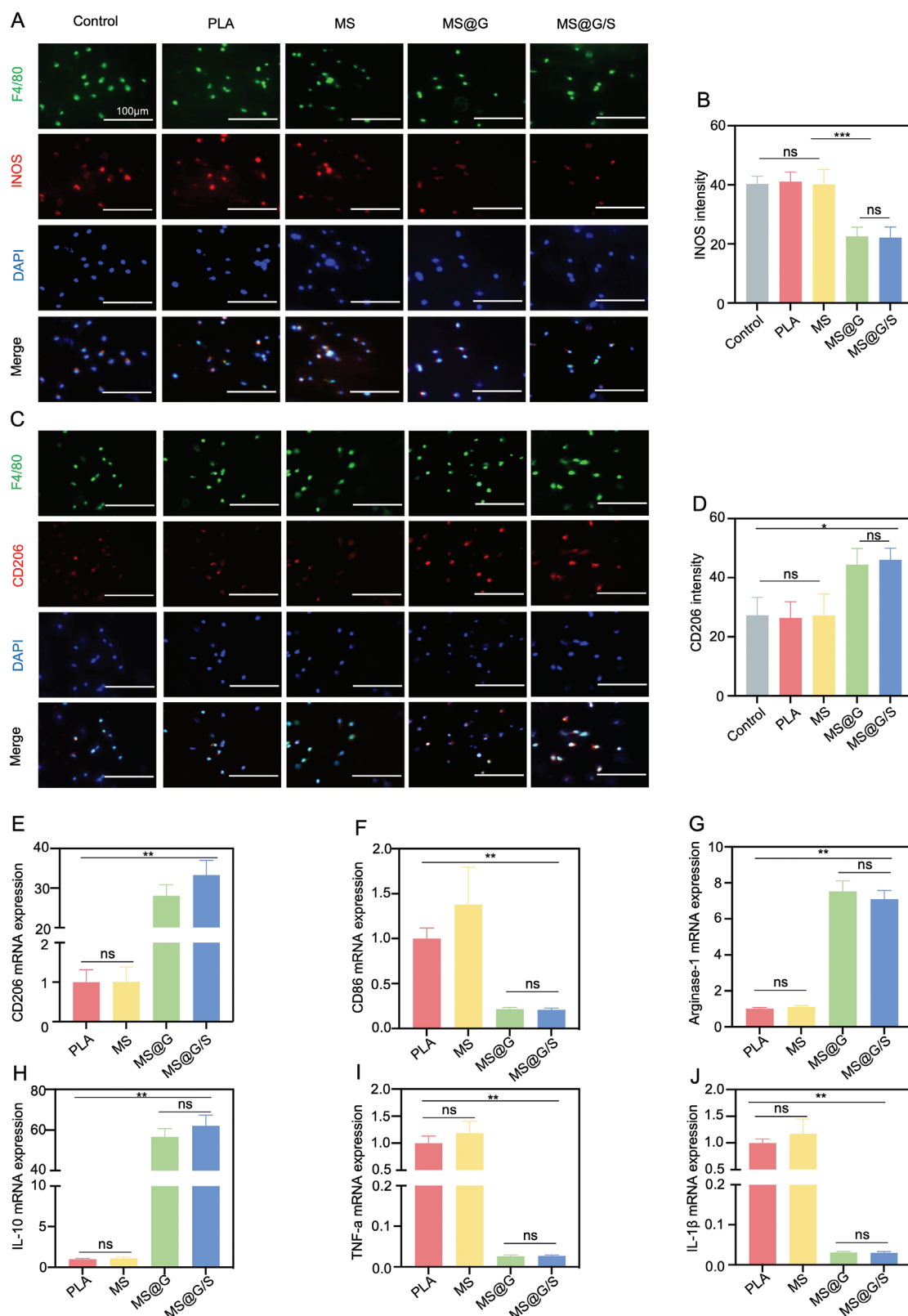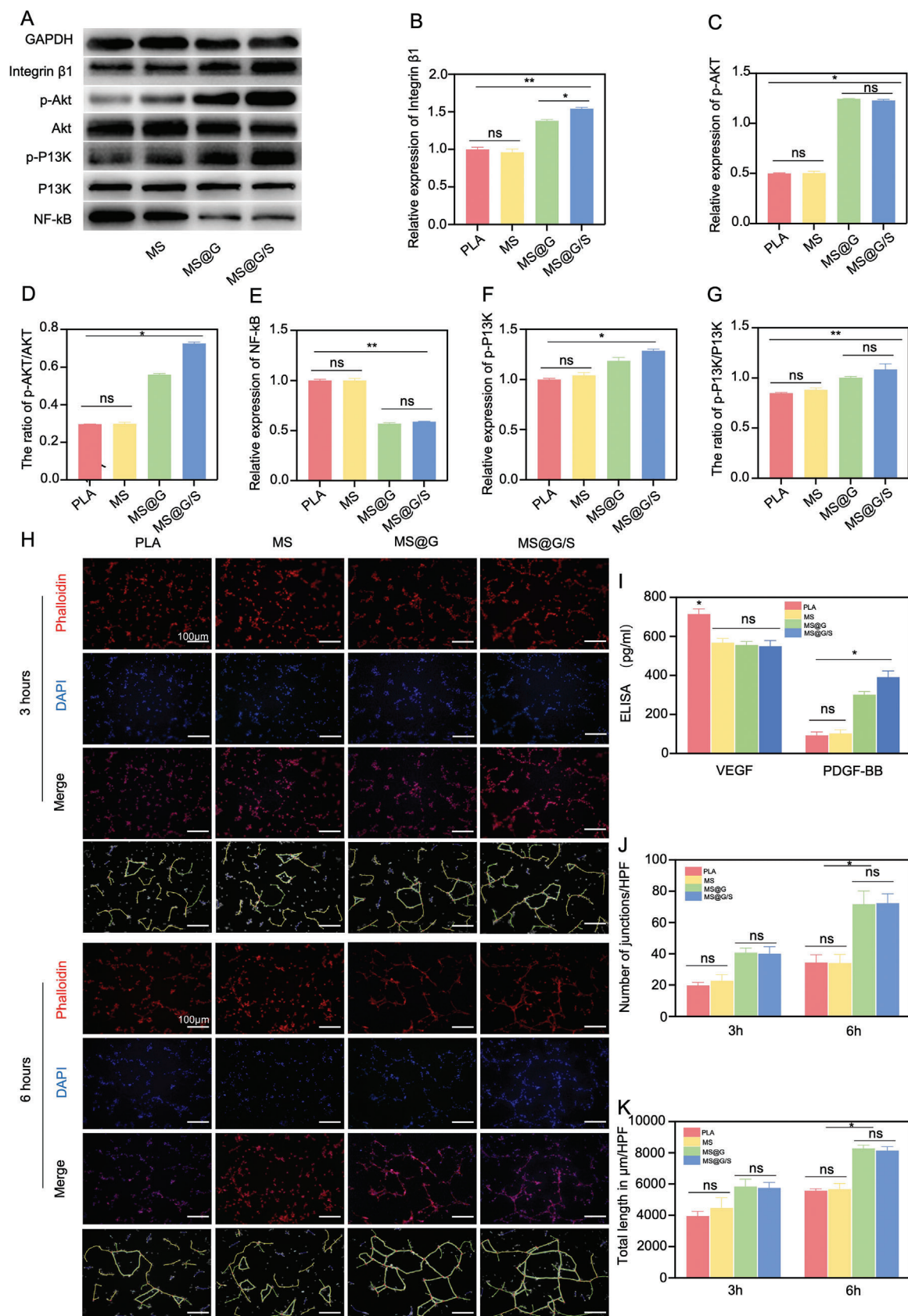
Figure 4. IF and PCR analysis of polarization on Mφ. A,C) Immunofluorescent staining of F4/80, CD206, and INOS at 7 days. B,D) Fluorescence intensity of INOS and CD206 at 7 days ($n = 3$). E,F) Expression analysis of CD206 and CD86 at 7 days. G–J) Expression analysis of inflammatory genes Arg-1, IL-10, TNF-α, and IL-1β at 7 days ($n = 5$) (all values were mean $\pm$ std. dev., statistical analysis evaluated by one-way analysis of variance (ANOVA) with Tukey's post-hoc test; ns, not statistically significant; *$p < 0.05$, **$p < 0.01$, ***$p < 0.001$).

ADVANCED
SCIENCE NEWS
www.advancedsciencenews.com

ADVANCED
HEALTHCARE
MATERIALS
www.advhealthmat.de

**ADVANCED
SCIENCE NEWS**

www.advancedsciencenews.com

**ADVANCED
HEALTHCARE
MATERIALS**

www.advhealthmat.de

($p < 0.05$), and the average tubular length at 3 and 6 h was 5943 ± 320 and 6247 ± 310 μm, respectively. These results indicated that both M1Mφ and M2Mφ play an indispensable role in the regeneration of blood vessels. However, M1Mφ secrete more VEGF in the early stage to accelerate the beginning of early vascularization. In contrast, M2Mφ secrete PDGF-BB and other factors, contributing to the maturation of vascular buds in the later stage.

These results suggested that the timely reprogramming of the immune microenvironment and the implementation of vascular regeneration aid in neural circuit reconstruction and promote nutrient metabolism of surviving tissues by alleviating ischemia and hypoxia. In this process, the initial triggering effect of early inflammatory reaction on tissue repair was confirmed, and the importance of the transformation from inflammation to an anti-inflammatory state was also pointed out.

Our in vitro angiogenesis experiments clarified that coagulated fiber scaffolds create a microenvironment suitable for tissue repair through macrophage paracrine effects, thereby boosting endothelial cell proliferation and vascular germination and maturation, indicating their potential efficacy in enabling the repair of damaged tissue.

2.8. Mφ-Transformed Microenvironment Regulates Neuronal Differentiation of NSCs

To investigate the long-term effects of Mφ on the differentiation of NSCs in the local microenvironment and the biological effects of BDNF-loaded fiber scaffolds, Mφ, NSCs, and different fiber scaffolds were cultured for 7 days using the Transwell coculture system (Figure 4B). NSCs in the bottom chamber were collected, and neurogenic differentiation was examined by immunofluorescence staining and qRT-PCR for Nestin, Neun, neural cytoskeletal tubulin (Tau), neuron-specific differentiated tubulin (Tuj-1), Map2, and GAP43. Immunofluorescence staining images showed that NSCs seeded on the fiber membrane presented a directional arrangement along the fiber distribution direction (**Figure 6**A). The fibrous membranes in the MS, MS@G, and MS@G/S groups (loaded with BDNF) showed neurogenic effects, and the seed cells (Figure 3C) showed neuron-like changes, that is, the appearance of axons and dendrites around the cell body. Cells disseminated on MS, MS@G, and MS@G/S fiber membranes exhibited strong green fluorescence signals, while fibers lacking BDNF (PLA) and controls showed weak green fluorescence signals. Semi-quantitative analysis revealed that the expression levels of neurogenic markers were increased in the BDNF-loaded groups (Figure 6B–F). These results indicated that microsol-electrospun fiber membranes release nerve growth factor and continuously promote neural differentiation of endogenous NSCs. Compared with the MS@G and MS@G/S groups, the MS group (coated with GelMA) gave a stronger green fluorescence signal. These results indicate that the presence of GelMA regulated the polarization of macrophages, reduced the inflam-

matory response, and promoted the neuronal differentiation of NSCs.

The qRT-PCR results were consistent with immunofluorescence results (Figure 6G–L). We observed a significant increase in the expression of neuron-specific marker genes in the BDNF-loaded and the GelMA-coated groups compared with the PLA group. BDNF provides nutrients for NSCs to differentiate from stem cells to mature neurons. This neurogenic effect of BDNF may cooperate with the regulation of the Mφ transformation microenvironment.

Together, these results show that coagulated fiber scaffolds exhibit specific biological characteristics in vitro. Their biocompatibility and microstructure provided padding for the defect site, and the scaffolds served as effective carriers of cells and cytokines. Through their modified hydrophilic surfaces and the sequential release of loaded drugs, the fiber scaffolds exerted effects on a variety of endogenous cells such as macrophages, HUVECs, and NSCs. They participated in reprogramming the neuroimmune microenvironment, the regulation of angiogenesis, and the differentiation of neuroblasts.

2.9. Recovery of Motor Function in Animals

The recovery of behavioral function is the goal of SCI repair. We next used a semi-sectioned SCI model of a Sprague–Dawley (SD) rat with injury at T9 to explore the performance of fiber bundles in vivo (**Figure 7**A). The Basso, Beattie, and Bresnahan (BBB) score and inclined plane test (IPT) score were used to evaluate the recovery of hindlimb motor dysfunction every week after SCI (Figure 7B,C).[34] The recovery of motor function in the MS@G/S group was better than that in the other groups; the BBB score at each time point from the fourth week after injury was significantly higher than those in the other groups. At week 8, the BBB and IPT scores in the MS@G/S group were $12.79 \pm 0.89°$ and $53.54 \pm 4.54°$, respectively, which showed obvious distinctions from the other groups. We further evaluated nerve repair by the minimum time required to achieve a motor function similar to that of pre-injury. We used a BBS score of 10 as the cutoff point and found that the MS@G/S group exceeded this cutoff as early as week 4, with a score of 10.42 ± 1.02. These results suggested that the MS@G/S implantable immunoregulatory fiber bundle not only effectively inhibits the acute inflammatory response of SCI and increases the survival likelihood of motor neurons but also promotes nerve regeneration in the later stage of SCI.

2.10. Evaluation of the Immune Microenvironment and Nerve Repair in Early SCI

NSCs can differentiate into neurons, astrocytes, and oligodendrocytes. Neurons play a crucial role in neural network reconstruction and normal function. Previous studies reported that NSCs

Figure 5. Polarization mechanism of Mφ and angiogenic paracrine on HUVECs. A) Phosphorylation levels of PI3K, Akt, and Protein expression level of integrin β1, NF κB by western blot. B–G) Quantitative analysis of phosphorylation levels of integrin, PI3K, Akt, and NFκB. H) Fluorescent staining of HUVECs vascularization under different Mφ/ electrospun fibers conditions. I) Detection of VEGF and PDGF-BB secreted by Mφ through ELISA. J,K) Quantitative analysis of junctions and tubular structure length (all values were mean ± std. dev. Statistical analysis evaluated by one-way ANOVA followed by Tukey's multiple comparison test (B–G,I) and two-way ANOVA followed by Tukey's multiple comparison test (J,K); $n = 3$, ns, not statistically significant; *$p < 0.05$; **$p < 0.01$).
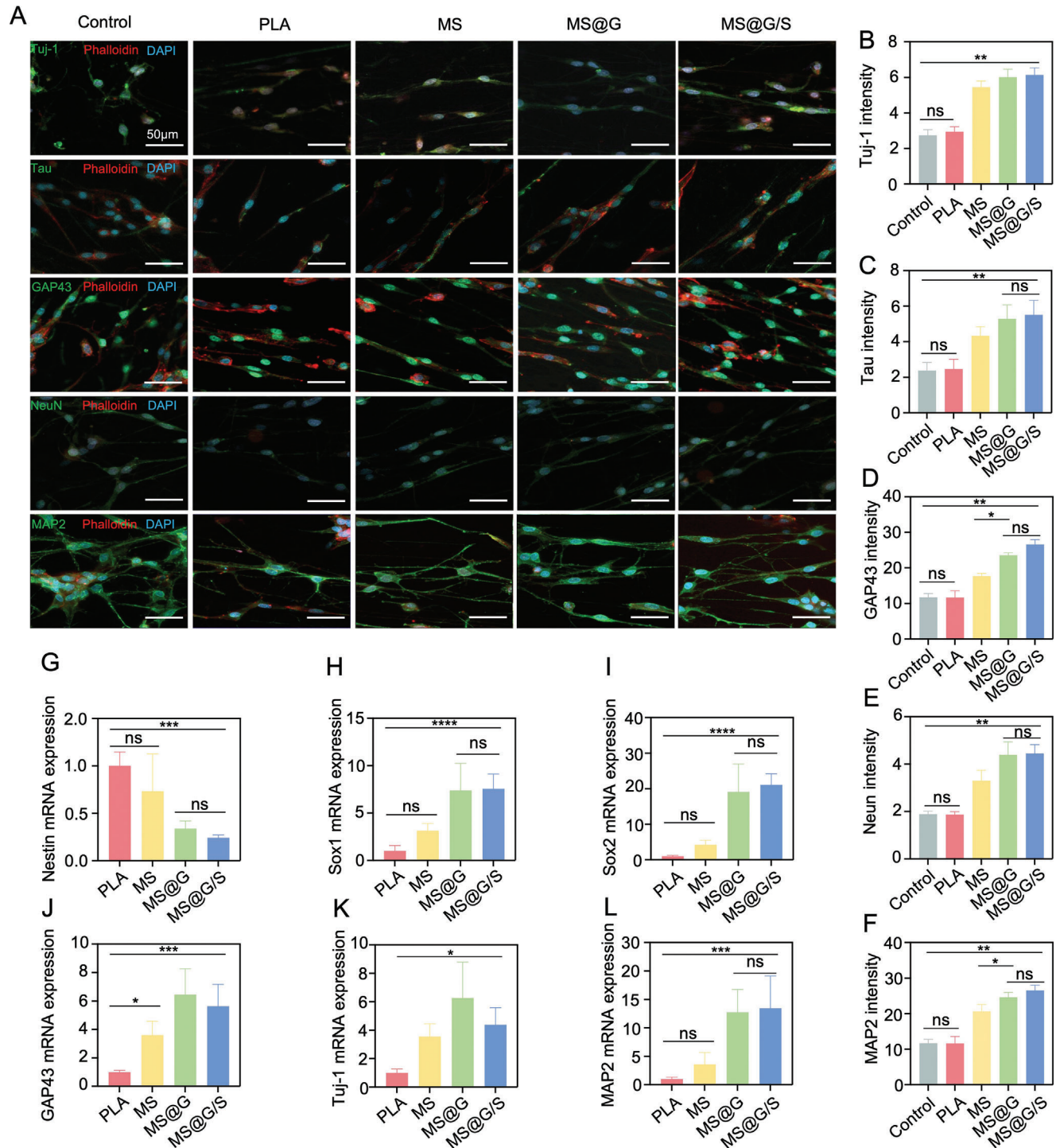
ADVANCED
SCIENCE NEWS
www.advancedsciencenews.com

ADVANCED
HEALTHCARE
MATERIALS
www.advhealthmat.de

Figure 6. IF and PCR analysis of Mφ/ NSCs. A) Immunofluorescence staining of Tuj-1, Tau, GAP43, NeuN, and MAP2 on different fiber scaffolds. B–F) Fluorescence semi-quantitative analysis of Tuj-1, Tau, GAP43, NeuN, and MAP2 ($n = 3$). G–L) mRNA expression analysis of Tuj-1, Nestin, GAP43, Sox1, Sox2, and MAP2 ($n = 5$) (all values were mean ± std. dev., statistical analysis evaluated by one-way analysis of variance (ANOVA) with Tukey's post-hoc test; ns, not statistically significant; *$p < 0.05$, **$p < 0.01$, ***$p < 0.001$, ****$p < 0.0001$).
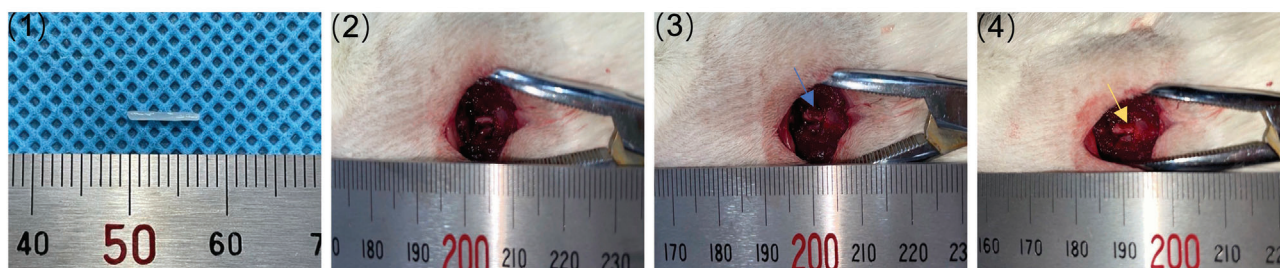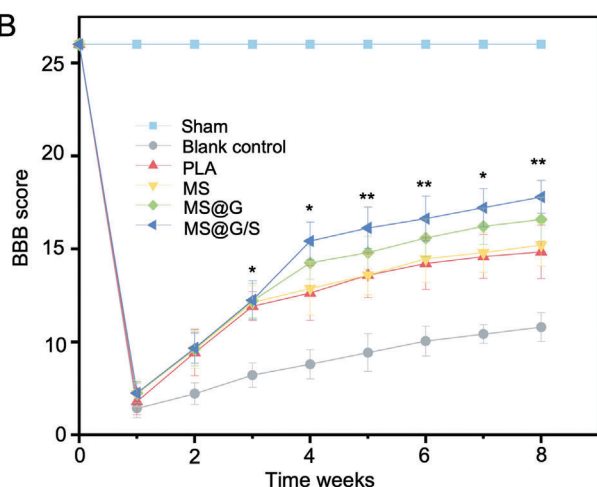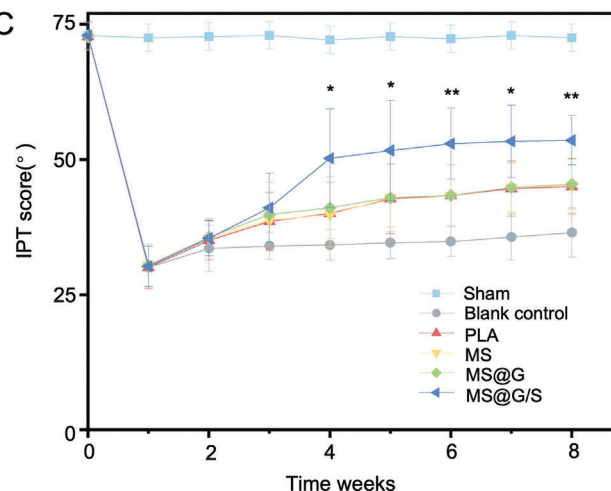
Figure 7. Animal experiment pictures and motor function scores. A) Animal experiment pictures, 1) image of the fiber scaffold, 2) complete exposure of the T9 spinal cord, 3) the correct 3 mm semi-transverse break on the T9 spinal cord (blue arrow indicated the injured spinal cord), 4) implanted fibrous bundle (yellow arrow indicated the location of the fibrous bundle implantation). B) BBB score for assessment of motor function recovery of the lower extremity. C) Motor function IPT score of rats (all values were mean ± std. dev., statistical analysis evaluated by two-way analysis of variance (ANOVA) with Tukey's post-hoc test; $n = 8$, $*p < 0.05$, $**p < 0.01$).

at the injury site are more inclined to differentiate into glial cells to form scar tissue under the influence of inflammation, which leads to difficulties in the reconstruction of neural circuits.[35] To solve this problem, researchers have attempted to identify strategies to modulate the microenvironment with the aim of promoting neuronal differentiation.

To examine NSC recruitment by SDF-1α release, we performed immunostaining for the NSC marker Nestin to trace endogenous NSCs at the lesion site 7 days after injury (**Figure 8**A). Compared with the absence of NSCs in the normal spinal cord, abundant NSCs appeared 7 days after stent implantation, suggesting rapid activation of NSCs after SCI. Quantification of the data showed that the MS@G/S composite scaffold recruited significantly more activated NSCs than the other groups (Figure 8F). These observations confirmed that the addition of SDF-1α to fibrous hydrogels rapidly and significantly enhances NSC recruitment at an early stage. The rapid recruitment of NSCs to the site of injury provides a critical resource for the reconstruction of damaged neural circuits.

On the 7th day after surgery, we examined the injury site using immunofluorescence. The paracrine status of the macrophages would change due to their subtype transformation ability.

To evaluate the polarization of Mφ, we performed immunostaining for INOS (M1 macrophages) and Arg-1 (M2 macrophages) (Figure 8B,C). The results showed that the PLA and MS groups showed stronger INOS staining, while in the MS@G and MS@G/S groups (with GelMA coating), Arg-1 staining was significantly stronger than INOS staining (Figure 8G,H). Staining for the macrophage subtype-specific cytokines TNF-α (M1-type cytokine) and IL-10 (M2-type cytokine) showed that TNF-α was expressed higher in the PLA and MS groups (the non-immune-regulated functional fiber scaffold group) than in the MS@G and MS@G/S groups ($p < 0.05$) (Figure 8D,E,I,J). IL-10 was expressed at higher levels in the MS-G and MS-G/S groups than in the other groups ($p < 0.05$). The MS@G/S group was more polarized to M2 than the MS@G group, which may be from the loss of some of the function of M1 because of the increased numbers of NSCs recruited by SDF-1α. Gao et al. found similar results, showing that iNSC affects microglial phenotypic activation neuroprotection through CXCL12/CXCR4 signaling.[36] This may also explain why the MS@G group showed no significant difference in the degree of M2 polarization with the MS@G/S group in the in vitro experiment; however, in the in vivo experiment, the MS@G/S group showed a stronger ability
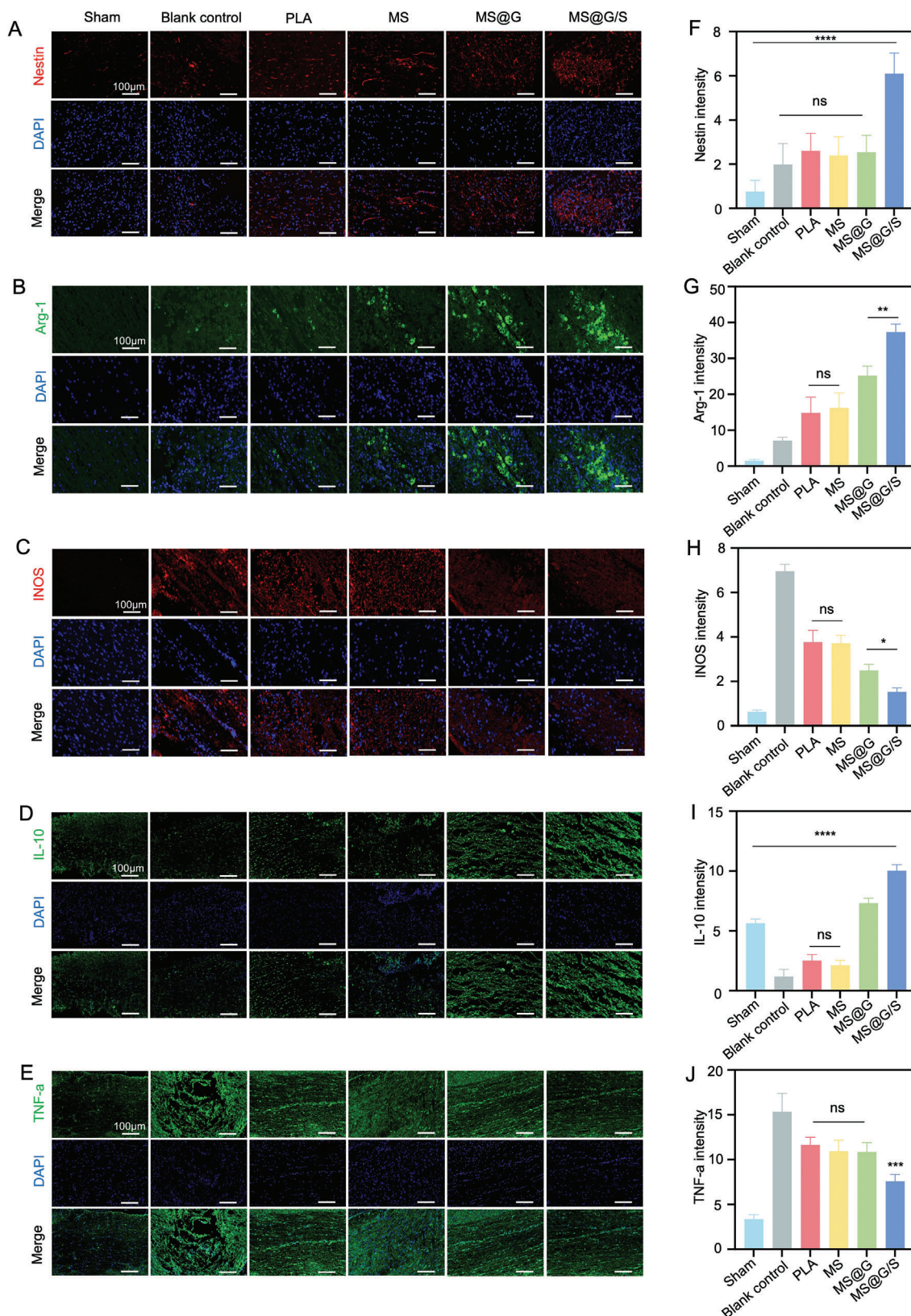
ADVANCED
SCIENCE NEWS

www.advancedsciencenews.com

ADVANCED
HEALTHCARE
MATERIALS

www.advhealthmat.de

Figure 8. Immunomodulatory evaluation 7 days after surgery. A–E) Nestin, Arg-1, INOS, IL-10, and TNF-α single immunofluorescence labeling. F–J) Quantitative analysis of Nestin, Arg-1, INOS, IL-10, and TNF-α immunofluorescence (all values were mean $\pm$ std. dev., statistical analysis evaluated by two-way analysis of variance (ANOVA) with Tukey's post-hoc test; $n = 5$, ns, not statistically significant; ***$p < 0.001$, ****$p < 0.0001$).

of M2 polarization. In general, the effect of the coagulation fiber scaffold on M2Mφ polarization attenuated the local inflammatory response. This timely shift in immune processes provided a neurogenic microenvironment conducive to differentiation activity.

2.11. Evaluation of the Immune Microenvironment and Nerve Repair in Advanced SCI

Secondary injury triggered by inflammation and chronic encapsulation of glial tissue prevents regenerating neurons and axons from penetrating and rebuilding the injured tissue, making neurogenic materials commonly reported to be in trouble. In the present case, the simultaneous introduction of immunomodulatory and neurogenic factors may inhibit the formation of glial tissue and promote nerve regeneration.[37] In the HE-stained samples (Figure S3A, Supporting Information) of the implanted fiber bundles, all material populations showed a much smaller spinal lumen area compared with the control group (Figure S3B,C, Supporting Information). However, dense glial tissue surrounding the fiber bundle was found in the PLA group. The MS group showed numerous parallel, red-stained collagen fibers and elongated fiber nuclei. In contrast, presumably from the immunomodulatory effects produced by the GelMA coating, the formation of glial tissue around the fiber tracts was reduced in both the MS@G and MS@G/S groups at 4 and 8 weeks after implantation.

After SCI, activated M1 microglia secrete IL-1α, C1q, and other inflammatory factors, which stimulate astrocytes to produce toxicity and accelerate scar tissue formation.[38] Acute inflammatory storms lead to the deposition of chondroitin sulfate proteoglycans in glial cells, resulting in glial scar tissue formation during secondary SCI and hindering nerve repair. To further investigate the immunoregulatory effects of fiber scaffolds on reducing scar formation, activated astrocytes and glial scar tissue were labeled with anti-GFAP antibody and anti-NG2 antibody, respectively (Figure S4A, Supporting Information). The amounts of activated astrocytes and glial scar tissue in PLA, MS, MS@G, and MS@G/S groups were significantly lower than those of the blank control group at 4 and 8 weeks. Studies have suggested that the directional electrospun fiber structure mimics the morphological distribution of neural tissue and increases the success rate of neural circuit reconstruction after nerve injury.

Semi-quantitative fluorescence analysis (Figure S4B,C, Supporting Information) showed that the signal intensity generated by MS@G/S fiber scaffolds was significantly lower than that of other control groups ($p < 0.05$). These results confirmed that the GelMA coating plays an immunomodulatory role and more effectively weakens inflammation, thereby reducing scar tissue formation and providing more possibilities for nerve repair. Furthermore, while scar tissue formation hinders cell migration from secondary SCI, the early release of SDF-1α from the MS@G/S scaffold rapidly recruits NSCs, thereby attenuating the adverse effects of scar tissue. Together, these results indicate that GelMA coating and SDF-1α not only pave the way for NSCs to migrate to the damaged area but also enable cells to reach the injury more quickly.

When SCI occurs, the blood-spinal cord barrier is damaged, and an ischemic and anoxic environment forms at the injury site. The germination and reconstruction of neovascularization enable the continuous transport of oxygen and nutrients to the injured tissue, which is essential for repairing tissue. Previous research has shown that the formation of neovascularization at the site of SCI promotes nerve regeneration.[39]

Immunofluorescence was performed at 4 and 8 weeks after injury; Von Willebrand factor (VWF) was used to label neovasculature, and CD31 was used to label endogenous cells (Figure S5A, Supporting Information). The quantitative results showed that the MS@G/S group contained a large amount of CD31-labeled vascular cells and positive VWF staining (for neovasculature) (Figure S5B,C, Supporting Information). The staining intensity for both compartments was significantly higher in the MS@G/S group than in the other groups. The amount of VWF-labeled neovascularization in the MS@G/S group at 4 weeks was significantly less than that at 8 weeks. Similarly, the number of CD31-labeled blood vessels was significantly higher at 8 weeks than at 4 weeks. This suggested that coagulate fiber scaffolds not only reduce the negative effect of inflammation and promote the polarization of M2 subtypes but also regulate the paracrine secretion of VEGF and PDGF-BB, promoting blood vessel maturation, and providing an excellent long-term guarantee for tissue regeneration. Luo et al. also found that M2 mediates vascular regeneration through exosomal OTULIN to promote the recovery of SCI.[40] In summary, our in vitro and in vivo results show that while M1 and M2 exhibit specific functions, M2 has advantages to some extent by regulating the polarization of Mφ, which could provide better vasculogenesis ability for SCI.

To track the fate of endogenous NSCs in the long term, Tuj-1, NeuN, and GAP43 were used to label neuronal cells and axon germination. These analyses can reveal nerve repair in the late stage of SCI. Endogenous stem cells were consistently promoted to differentiate into neurons by programmed release of BDNF from microsol-electrospun fibers (MS, MS@G, and MS@G/S), as indicated by the high expression of Tuj-1 and NeuN at 4 and 8 weeks (**Figure 9**A,C,D). Moreover, the expression of Tuj-1 and NeuN in the microsol-electrospun fiber group (MS, MS@G, and MS@G/S) was significantly higher than that of the other groups in the same period, and staining at 8 weeks was significantly higher than that at 4 weeks. These results further proved that the coagulated fiber scaffold continuously promotes nerve regeneration. In the MS@G/S group, astrocyte toxicity and scar tissue formation were significantly reduced because of GelMA-coated immunomodulation. Thus the number of neurons was significantly greater than in the other groups at both time points.

These results confirmed that the coagulated fiber scaffold had immunomodulatory capacity in SCI and provides continuous differentiation information for nerve regeneration through its spatiotemporal delivery system loaded with BDNF. Studies have shown that there is a limited time window for SCI repair.[41] The expression of GAP43 in the spinal cord reflects an active degree of the spinal cord. Under normal conditions, the expression of GAP43 is low in the spinal cord; in the presence of SCI, GAP43 is highly expressed to promote axonal elongation and release neurotransmitters. However, the high expression of GAP43 did not persist, which was consistent with the limited time window of SCI repair. At each examined time point, GAP43 expression was
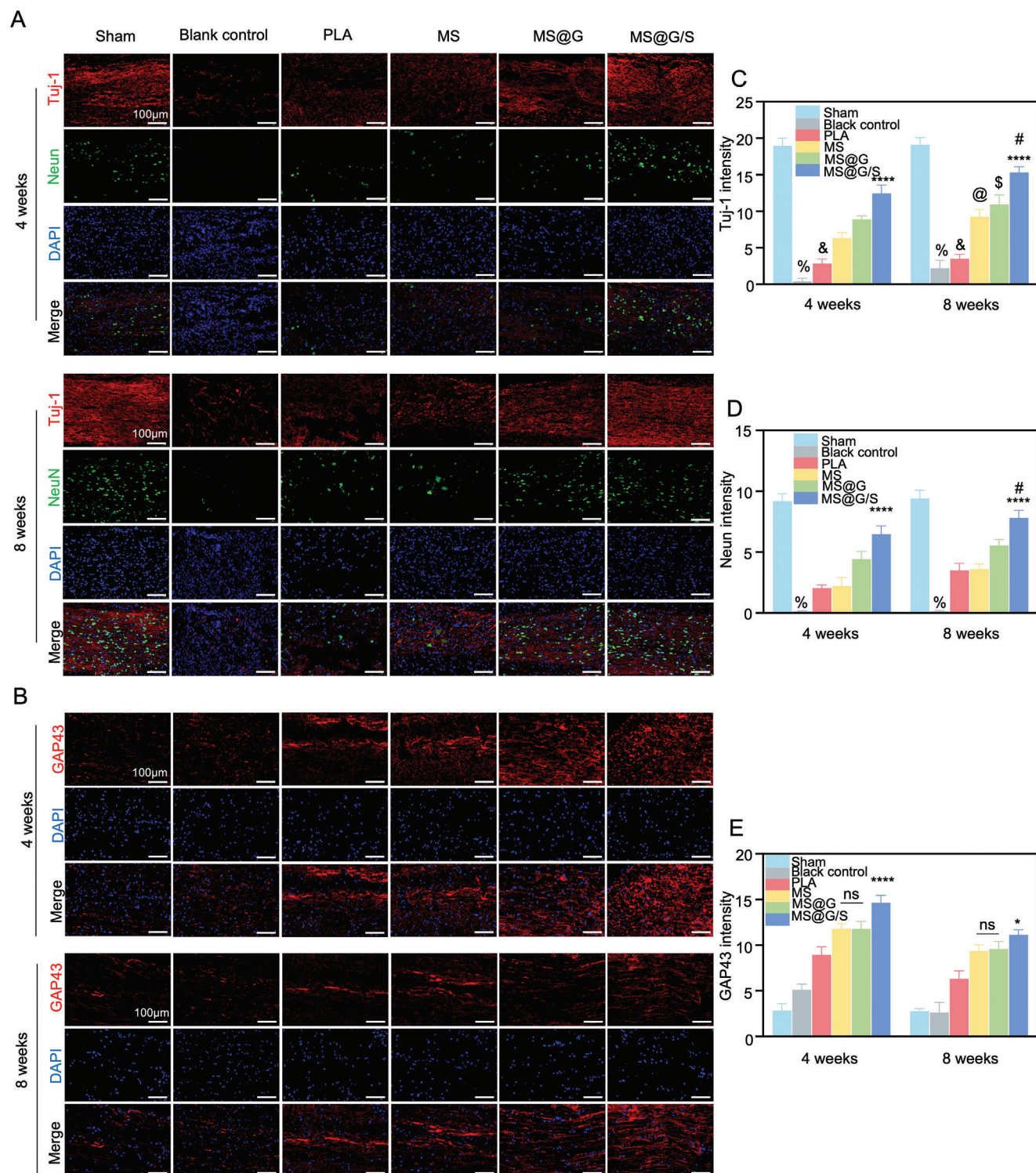
Figure 9. Immunofluorescence staining of neuronal cells and axons. A,B) Immunofluorescence staining of neuronal cells and axons at 4 and 8 weeks. C–E) Quantitative analysis of optical density for Tuj-1, Neun, and GAP43. ($n = 5$, all values were mean ± std. dev., %$p < 0.001$ when comparing blank control and microsol-electrospun groups (MS, MS@G, and MS@/S); &$p < 0.05$ when comparing PLA and microsol-electrospun groups (MS, MS@G, and MS@/S); @$p < 0.01$ when comparing 4w and 8w in MS; $$p < 0.01$ when comparing 4w and 8w in MS@G and #$p < 0.01$ when comparing 4w and 8w in MS@G/S; *$p < 0.05$, ****$p < 0.0001$ when comparing MS@G/S and other control groups at the same time point via two-way analysis of variance (ANOVA) with Tukey's post-hoc-test).

**ADVANCED
SCIENCE NEWS**

www.advancedsciencenews.com

**ADVANCED
HEALTHCARE
MATERIALS**

www.advhealthmat.de

significantly higher in the MS@G/S group than in the control groups; GAP43 staining in the sham group was lower than in the other groups (Figure 9B,E). However, the expression of GAP43 in all experimental groups at 4 weeks was significantly higher than that at 8 weeks; this was not observed in the sham-operated group. This suggested that reducing the inflammatory response in the acute phase through immune regulation may better promote nerve regeneration in the limited time window of SCI recovery.

Our in vitro results showed that the coagulation scaffolds could guide macrophages to M2Mφ polarization to reduce the formation of scar tissue, promote angiogenesis through paracrine VEGF and PDGF-BB effects, and reprogram the immune microenvironment for tissue repair and neurons for the early and rapid recruitment of NSC and subsequent differentiation, all of which exhibit beneficial treatment effects.

3. Conclusion

In this study, we developed a strategy to regulate acute inflammation and recruit and promote the differentiation of endogenous NSCs to guide the recovery of nerve function after SCI. From a covalent network formed by the active carboxyl group resulting from PLLA hydrolysis and GelMA amino group, the constructed coagulate composite fiber had high hydrophilicity, programmed delivery of loaded cytokines, and other characteristics that made it suitable for the complex and variable pathological microenvironment of SCI. This stable, flexible, and rigid structure showed improved hydrophilic properties compared with traditional PLLA. MS@G/S exhibited high hydrophilicity, enhanced the integrin receptor expression on macrophage surfaces, activated the PI3K/AKT signaling pathway, inhibited NF-κB activation, and polarized macrophages to M2 anti-inflammatory macrophages. The influence of coagulation fibers on regulating the local immune response was demonstrated using a rat model of SCI. The combined effect of GelMA degradation and MS diffusion with the spatiotemporal release of SDF-1α and BDNF induced endogenous NSCs to home along the gradient and differentiate into neurons. In conclusion, these biomimetic coagulation composite fibers, which exhibit both anti-inflammatory and repair properties, may represent a new resource for developing treatments for SCI.

4. Experimental Section

Preparation of PLA and MS Spinning Solution: PLLA (Idle Gang, China) in 4 g dichloromethane (DCM) (Aladdin, China) and 2 g *N,N*-dimethylformamide (DMF) (Qiang Shun, China) were combined with magnetic stirring at room temperature to obtain a pure PLA electrospinning solution. MS electrospinning solution was prepared using 1 wt% sodium hyaluronate pure sol. Sodium hyaluronate sols were dissolved in 9.9 g deionized water with 0.1 g HA and rotated to completely dissolve at room temperature. Homogeneous HA-BDNF hydrosol was obtained by mixing 10 µL rat BDNF (100 µg mL^{-1}) (PeproTech, USA) with 50 µL HA solution. Then, 0.01 g Span80 (Sigma, USA) and 4 g DCM were added to the mixture with uniform stirring. Finally, 0.5 g PLA and 2 g DMF were added to obtain the MS spinning solution.

Preparation of Different Directional Electrospun Fibers: To prepare electrospun fiber, the electrospinning solution was loaded into syringes (10 cm in length, inner diameter of 0.9 mm, and volume of 10 mL). The syringe was fixed on the propulsion pump and the speed was set to 70 µL min^{-1}. The needle end was fixed with the metal clip of a DC high-voltage power supply; the voltage was set to 16 kV, and the distance between the needle tip and the parallel electrode receiver was ensured to be 20 cm. Parallel-oriented fiber scaffolds (PLA and MS) were collected in-between electrode rods. The prepared electrospun fibers were dried overnight in a vacuum oven to remove residual organic solvents. Oriented fiber membranes were used for in vitro research and fiber scaffolds were used for in vivo research.

Preparation of MS@G/S: After previous studies, a basic alkaline solution was prepared, and 10 mL of 0.1 M NaOH (Aladdin, China) solution was compounded with an equal volume of ethanol. The electrospun fibers were hydrolyzed in the solution for 30 s at room temperature and then carefully rinsed with deionized water. To activate the carboxyl group on the hydrolyzed fibers (PLA, MS), the electrospun filaments were immersed in a mixture containing 40 mg 1-(3-dimethylaminopropyl)-3-ethylcarbodiimide hydrochloride (EDC), 60 mg *N*-hydroxy succinimide, and 5 mL MES (pH = 6) buffer (Aladdin, China). Electrospun filaments were held at 37 °C for 15 min and rinsed with deionized water after removing the supernatant. GelMA (60% substitution, EFL, China) and deionized water containing photoinitiator in a 10% GelMA solution were prepared, and SDF-1α (PeproTech, USA) was directly added to a concentration of 200 µg mL^{-1}. The treated electrospun filaments were then immersed in GelMA solution containing SDF-1α and held to react overnight at 37 °C. Finally, the electrospun filaments were removed from the solution and photo-crosslinked with UV irradiation (365 nm, 6.9 mW cm^{-2}) to embellish the surface. The electrospun filaments were freeze-dried and stored.

SEM: The fiber scaffolds were attached to a copper plate with a conductive adhesive and placed on the sample table of the SEM (Hitachi, Japan) under a vacuum state after ion-sputtering gold plating. The voltage was set to 10 kV, and the fiber scaffold was photographed and recorded. ImageJ was used to process images and calculate the fiber diameters of fiber scaffolds; Origin9.0 was used to draw histograms of the results.

TEM: PLA and MS were collected on a duplex copper mesh (Zhongjing Koyi, China) and dried at room temperature. The fiber morphology and internal structure were observed by TEM at 120 kV (Hitachi, HT7700, Japan).

EDS: PLA, MS, and MS@G/S were analyzed with EDS (FEI, USA) to evaluate the chemical elements on the surfaces.

FTIR: The fiber membranes of different groups were scanned 128 times by ATR-FTIR (Thermo Scientific, USA). The changes in chemical bonds during the modification were analyzed using the obtained curves.

XPS: Changes in the elements and chemical bonds of MS@G/S caused by the modification process were detected with XPS (Thermo Scientific Escalab, USA).

Tensile Test and Young's Modulus Measurement: A strip of 15 × 3 × 0.1 mm was made from the fiber membrane of each group with a mold. The strips were measured by a mechanical testing machine (Shanghai Hengyi Precision Instrument Co., LTD., China) at a speed of 2.5 mm min^{-1} and the mechanical tensile curves were drawn.

Water Contact Angle Measurement: Water contact angles were evaluated to assess the hydrophilicity/hydrophobicity of different fiber membranes; angles were determined by measuring the angle of a drop of water on the fibers using a contact angle meter (Data Physics Corporation, DSA25S, Germany). A smaller water contact angle indicated better hydrophilicity of the material.

Particle Size Analysis: DLS (Malvern, UK) was used to analyze the size distribution of HA microsol particles dispersed in methylene chloride.

Determination of Porosity: The porosity of each fiber scaffold was measured by the pycnometer method.[42] The weight of the pycnometer containing ethanol was measured as W1. A sample, with a weight (Ws), was immersed in ethanol and then saturated with ethanol. After adding ethanol to fill the specific gravity bottle, the pycnometer was weighed as W2. The ethanol-filled sample was removed from the pycnometer and the residual weight of the ethanol, and the specific gravity flask was measured, as W3. The porosity of the membrane was then calculated using Equation (1)

$$ p = \frac{W2 - W3 - Ws}{W1 - W3} \times 100\% \tag{1} $$

Cytokine Release: For the release assays, MS@G/S fiber membranes (10 mg MS, theoretically containing 20 ng BDNF, and deliberately loaded with GelMA coating containing 20 ng SDF-1α) were immersed in 10 mL of 1% BSA in a 50-mL centrifuge tube. The tube was placed in a constant temperature vibrator at 37 °C at 100 cycles min^{-1}. At specified time points (0.5, 1, 2, 4, 6, 8, 10, 14, 18, 23, and 28 days), the release buffer was collected from the centrifuge tube; after buffer collection, 10 mL fresh PBS was replaced and vibration continued. The concentrations of BDNF and SDF-1α in the release buffer were measured using a BDNF ELISA kit (R&D Systems, USA) and an SDF-1A ELISA kit (R&D Systems, USA), respectively.

To visualize the presence and distribution of cytokines in core–shell structures, fluorescent electrospinning solutions were fabricated with fluorescein isothiocyanate (FITC)-labeled bovine serum albumin (Solarbio, Beijing, China) instead of BDNF coated with microsol. The electrospun fibers were collected and viewed with a fluorescence microscope (Carl Zeiss, USA).

Cell Culture: Primary rat NSCs were isolated from the brain of E14 fetal rats by staff at the Institute of Orthopedics of the First Affiliated Hospital of Soochow University. Fetal rats were removed from the abdomen of 14-day pregnant rats under anesthesia (2% pentobarbital) soaked in 75% alcohol for 2 min. The rats' heads were separated under sterile conditions to dissect the brains. The meninges and blood vessels were removed from the pre-cooled dissecting fluid, and the lateral ventricles and hippocampal gyrus were removed; the tissues were cut into pieces. The samples were transferred to a Petri dish; 2 mL 0.25% trypsin was added, and the sample was digested in an incubator at 37 °C for 25 min. Next, the tissue fragments were transferred to a centrifuge tube, and the sample was centrifuged at 1000 rpm min^{-1}; the solution was discarded, the precipitate was washed thrice with PBS, and the supernatant was discarded. Next, the tissue block was blown with 1 mL of NSC medium (Procell, China). After repeating 3–4 times, the tissue was digested, and the final residue was discarded. Single-cell suspensions were collected and seeded in 6-well plates at 1×10^7 cells per well. NSCs were cultured in a complete culture medium of NSCs (Procell, China).

Primary rat BMSCs were obtained from rat femurs and tibias after isolation and culture; cells were cultured in α-MEM medium (Thermo Fisher Scientific, USA). Rat Mφ were purchased from Wuhan Procell Life Science and Technology Co. and cultured in RPMI-1640 medium (Procell, China). HUVECs were purchased from Shanghai Fuhang Materials Technology Co., LTD., China, and cultured in DEME/F12 medium (Procell, China). All cells were cultured at 37 °C, 95% relative humidity, and 5% CO_2. The medium was changed every 2–3 days, and growth status was monitored when changing the medium. Electrospun membranes (100 µm thick) were placed on 15 mm glass coverslips and irradiation-sterilized for cell culture on fiber scaffolds. The cells were inoculated on different electrospun fibers with the indicated number of cells and cultured.

Determination of Cell Viability: The viability of bone marrow mesenchymal stem cells on fibrous membranes was detected by live/dead fluorescence staining. BMSCs (1×10^4) were seeded in 24-well plates preloaded with different fibrous membranes and cultured for 3 days. First, cells were stained with live/dead cell working staining solution (Invitrogen, USA) for 30 min in the dark at 27 °C. Then, the solution was removed, and cells were observed under a fluorescence microscope (Carl Zeiss, USA).

Cell Proliferation Assay: Cells were plated into 24-well plates (1×10^5 cells per well). CCK-8 reagent (Dojindo, Japan) was added to the medium (at a ratio of 1:9), and the medium was changed at set time points (1, 3, 5, and 7 days). After 4 h of incubation in the cell culture incubator, 100 µL of the mixture was transported into 96-well plates before being measured by a microplate reader.

Adhesion Ability of Cells: Immunofluorescence staining was performed to confirm the potential mechanism of the altered adhesion caused by the increased surface hydrophilicity of the fiber scaffolds.

BMSCs were co-cultured on different electrospun fibers for 24 h. The medium was removed, and BMSCs were fixed with 4% paraformaldehyde for 1 h. Next, cells were washed with PBS, and 0.3% Triton was used for cell perforation for 30 min. After three washes, the cells were incubated with a rapid closure solution (Beyotime, China) for 1 h. After three washes, cells were incubated with primary antibodies against integrin β1 (Novus, USA)

overnight at 4 °C. The next day, cells were washed three times and incubated with a secondary antibody (Abcam, USA) at 37 °C for 2 h. Finally, phalloidin and DAPI stained the cytoskeleton and nucleus, respectively. Cells were observed and photographed using an inverted fluorescence microscope. Image J software was used to semi-quantify fluorescence intensity.

Confirmation of NSCs: As described above, cells obtained from fetal rat brains were cultivated for 3 days until neurosphere formation was detected under a bright field microscope. Cells were then stained for the NSC marker Nestin by immunofluorescence staining. Cells were fixed, permeabilized, washed, and then blocked with BSA (5% W/V) (Biosharp, China) overnight at 4 °C. Cells were incubated with primary antibodies against Nestin (Novus, USA) overnight at 4 °C, followed by three washes in PBS. Cells were stained with secondary antibodies (Jackson, USA) at room temperature and washed three times in PBS. Phalloidin and DAPI were used to stain the cytoskeleton and nucleus, respectively. NSCs were observed under a fluorescence microscope.

Cell Migration Assay: To evaluate the recruitment ability of SDF-1α uniformly dispersed in GelMA coating, an 8-µm Transwell (Corning, USA) chamber was used to assess cell migration. NSCs (5×10^5) were placed in the upper chamber, and different fiber membranes were placed in the lower chamber. SDF-1α was used as a positive control. Cells were incubated for 24 h. The chambers were then immersed in 4% paraformaldehyde and fixed for 20 min; after washing three times with PBS, the cells were permeabilized with Triton for 15 min. After washing again, the cells were stained with 1% crystal violet dye solution (Beyotime, China) for 20 min. Finally, the remaining cells in the chamber were scraped off with a cotton swab, and the cells on the side and bottom surface outside the chamber were retained (as migrated NSCs). The cells were observed under a bright field microscope, and ImageJ software was used to count the migrated NSCs.

Mφ Phenotype Analysis: Mφ (at a concentration of 5×10^4 mL^{-1}) were inoculated on PLA, MS, MS@G, and MS@G/S scaffolds. After 7 days of culture, cells were harvested and incubated with anti-CD45-FITC (BD Pharmingen, USA), anti-CD11B-PECy7 (BD Pharmingen, USA), anti-CD86-APC (BD Pharmingen, USA), and anti-CD206-PE (BD Pharmingen, USA) at 4 °C for 30 min in the dark and then analyzed by flow cytometry (Merck Millipore, Germany) and FlowJo software. Myeloid cells were first circled by CD45 and CD11b, followed by CD86 and CD206 positive cells. In other experiments, Mφ (at a density of 5×10^4 mL^{-1}) was co-cultured with fiber membranes for 7 days. Cells were then stained with F4/80 (Abcam, AB100790), INOS (Abcam, AB49999), and CD206 (Santa Cruz, SC-376108) antibodies. Next, Mφ were fixed, blocked, and incubated with primary antibody, secondary antibody, and DAPI as described above; stained cells were observed and photographed under an inverted fluorescence microscope.

Western Blot: RIPA lysate (Beyotime, China) was used to extract total cell proteins of Mφ, and the protein concentrations were quantified using the BCA protein concentration assay kit (Solarbio). Equal amounts of protein (20 µg) were separated using 10% SDS-PAGE and transferred to membranes. After blocking, the membranes were incubated with primary antibodies against integrin β1 (Abcam, AB179471), p-Akt (CST, 4060T), Akt (Abcam, AB179463), P-P13K (Abmart, T40065), P13K (Abcam, AB191606), NF-κB (CST, 8242T), and GAPDH (CST, 5174T), followed by incubation with secondary antibody (ABclonal, USA). Bands were detected using an ECL luminescent kit and gel imaging system.

ELISA: Mφ were cultured with different electrospun fibers for 7 days, and then, the supernatant of the cell culture medium was collected. The levels of VEGF and PDGF-BB in cell culture supernatant were detected by ELISA kits (Elabscience, China). Concentrations were calculated from a standard curve.

HUVEC Tube Forming Assay: Mφ were cultured with different electrospun fibers for 7 days. First, the supernatant of the cell culture medium was collected and mixed with the HUVEC culture medium at a ratio of 1:1 to prepare the HUVEC-specific medium. Next, on ice, 24-well plates were coated with low growth factor matrix gel (150 µL per well, Corning, USA). Finally, HUVECs (1×10^5 cells per well) were seeded, and the HUVEC-specific medium was added. After 3 and 6 h of incubation, the HUVECs were fixed, permeabilized, and closed. Phalloidin and DAPI were used to

2202658 (19 of 21)

stain the cytoskeleton and nucleus, respectively, and HUVECs were observed under an inverted fluorescence microscope.

Neurogenic Differentiation: In Transwell chambers, fiber scaffolds + Mφ were co-cultured in the upper chamber, and fiber scaffolds + NSCs were co-cultured in the lower chamber for 7 days. NSCs were then subjected to immunofluorescence staining for Neun (Abcam, USA, AB177487), Tau (Abcam, USA, AB80579), TUJ-1 (Abcam, USA, AB18207), Map2 (Abcam, USA, AB183830), and GAP-43 (Abcam, USA, AB75810) as described above. Imaging was performed with a confocal microscope (Carl Zeiss, USA), and Image J was used for semi-quantitative analysis of fluorescence intensity.

qRT-PCR: The gene expressions of specific markers of neurons and Nestin, Sox1, Sox2, Tuj-1, Map2, and GAP43 were examined in neuron-like cells after 7 days of co-culture. In addition, the gene expressions of Mφ, including CD206, CD86, arginase-1, IL-10, TNF-α, and IL-1β, were detected to assess the polarization of Mφ. Total RNA was extracted from Mφ and NSCs with Trizol reagent (Invitrogen, USA) and subjected to reverse transcription using a reverse transcription kit (Takara, Japan). qRT-PCR was then performed using a polymerase chain reaction kit (Takara, Japan). Glyceraldehyde-3-phosphate dehydrogenase (GAPDH) mRNA was used as a reference. Genewiz Biotechnology Co., LTD designed and synthesized the primers (Tables S1 and S2, Supporting Information).

Animals: SD male rats (200–250 g) were obtained from Zhaoyan (Suzhou) New Drug Research Center Co., Ltd. The Ethics Committee of Soochow University approved all surgical operations and perioperative treatments (Approval No. SUDA20221207A01).

Establishment of the Spinal Cord Hemisection Model: SD rats were anesthetized by intraperitoneal injection of 2% sodium pentobarbital (50 mg kg^{-1}). A 3-cm longitudinal incision was made on the back of the rat centered at T9, taking care to preserve the subcutaneous fat pad (which contained a rich blood supply). After carefully separating the paravertebral muscles, the T9 lamina was fully exposed in the spinal canal. The right lamina was opened to expose the spinal cord, and the right side of the spinal cord was cut with a medical blade to create a spinal cord defect in 3 mm halves. After saline lavage, 2 mm × 2 mm × 3 mm fiber bundles were placed in the injured area. The muscles and skin were sutured layer by layer; penicillin (2 × 10^5 units, KEDA, China) was intramuscularly injected daily for 7 days, and the bladder was manually emptied every 12 h. The sham group underwent a simple laminectomy, and the blank control group underwent spinal cord hemisectomy without implantation material. The negative control group was implanted with different fiber scaffolds PLA, MS, and MS@G.

Assessment of Animal Motor Function: The recovery of hindlimb nerve motor function was evaluated in the open field. The BBB score was used to numerically evaluate the motor function of rats, with scores ranging from 0 to 21. As a complementary study to the BBB score test and to improve the validity of the results, IPT scoring was used. The rats were placed on an inclined plate, and the maximum tilt angle that the rats could withstand was recorded. A greater angle indicated a greater carrying capacity of the lower limbs. Eight rats from each group were randomly selected at specific time points each week for evaluation; three blinded observers determined the BBB score and IPT score.

Specimen Collection: At postoperative 1, 4, and 8 weeks, 10 rats in each group were randomly selected and euthanized. Spinal cord specimens were collected, fixed with 4% paraformaldehyde for 24 h, subjected to gradient dehydration, immersed in absolute ethanol xylene solution and pure xylene solution, and embedded in paraffin. Longitudinal sections of 5 μm were generated from paraffin blocks of each group using a microtome and used for histological analysis.

Histological Analysis: Tissue sections were stained with H&E to analyze syringomyelia in the defect area. In addition, immunofluorescence staining and immunohistochemical staining were performed using the following antibodies: INOS (Abcam, AB283655), Arg-1 (Abcam, AB203490), IL-10 (Abcam, AB9969), and TNF-α (Abcam, AB6671) were used to assess early macrophage polarization; Nestin (Abcam, AB221660) was used to assess the early recruitment of endogenous NSCs; GFAP (Service Bio, GB12096) and NG2 (Abcam, AB50009) were used to evaluate the formation of glial scar at 4 and 8 weeks; CD31 (Service Bio, GB12063) and VWF

(Abcam, AB6994) were used to assess angiogenesis at 4 and 8 weeks; and Tuj-1 (Abcam, AB18207), GAP43 (Abcam, AB75810), and NeuN (Abcam, AB177487) were used to evaluate nerve repair in the middle and late stages.

Statistical Analysis: All experimental data results are expressed as mean ± standard deviation. Graph Prism 9.3 and Origin 9.1 software were used to analyze and plot. The differences between groups were tested by One-way or two-way analysis of variance and Tukey's multiple comparison methods. Differences with statistical significance were marked by *p < 0.05, **p < 0.01, ***p < 0.001, and ****p < 0.0001, and differences with no statistical significance were marked by ns.

Supporting Information

Supporting Information is available from the Wiley Online Library or from the author.

Conflict of Interest

The authors declare no conflict of interest.

Data Availability Statement

Research data are not shared.

[1] J. W. McDonald, C. Sadowsky, *Lancet* **2002**, *359*, 417.

[2] a) D. J. Hellenbrand, C. M. Quinn, Z. J. Piper, C. N. Morehouse, J. A. Fixel, A. S. Hanna, *J. Neuroinflammation* **2021**, *18*, 284; b) A. Anjum, M. D. Yazid, M. F. Daud, J. Idris, A. M. H. Ng, A. S. Naicker, O. H. R. Ismail, R. K. A. Kumar, Y. Lokanathan, *Int. J. Mol. Sci.* **2020**, *21*, 7533; c) M. Karsy, G. Hawryluk, *Curr. Neurol. Neurosci. Rep.* **2019**, *19*, 65.

[3] M. B. Orr, J. C. Gensel, *Neurotherapeutics* **2018**, *15*, 541.

[4] B. Fan, Z. Wei, X. Yao, G. Shi, X. Cheng, X. Zhou, H. Zhou, G. Ning, X. Kong, S. Feng, *Cell Transplant.* **2018**, *27*, 853.

[5] Y. Yang, Y. Fan, H. Zhang, Q. Zhang, Y. Zhao, Z. Xiao, W. Liu, B. Chen, L. Gao, Z. Sun, X. Xue, M. Shu, J. Dai, *Biomaterials* **2021**, *269*, 120479.

[6] a) R. Shechter, A. London, C. Varol, C. Raposo, M. Cusimano, G. Yovel, A. Rolls, M. Mack, S. Pluchino, G. Martino, S. Jung, M.

Schwartz, *PLoS Med.* **2009**, *6*, e1000113; b) F. H. Brennan, Y. Li, C. Wang, A. Ma, Q. Guo, Y. Li, N. Pukos, W. A. Campbell, K. G. Witcher, Z. Guan, K. A. Kigerl, J. C. E. Hall, J. P. Godbout, A. J. Fischer, D. M. McTigue, Z. He, Q. Ma, P. G. Popovich, *Nat. Commun.* **2022**, *13*, 4096.

[7] J. Van Broeckhoven, D. Sommer, D. Dooley, S. Hendrix, A. Franssen, *Brain* **2021**, *144*, 2933.

[8] M. Stenudd, H. Sabelström, J. Frisén, *JAMA Neurol.* **2015**, *72*, 235.

[9] H. Shen, C. Fan, Z. You, Z. Xiao, Y. Zhao, J. Dai, *Adv. Funct. Mater.* **2022**, *32*, 2110628.

[10] a) Q. Zhang, B. Shi, J. Ding, L. Yan, J. P. Thawani, C. Fu, X. Chen, *Acta Biomater.* **2019**, *88*, 57; b) A. D. Schoenenberger, H. Tempfer, C. Lehner, J. Egloff, M. Mauracher, A. Bird, J. Widmer, K. Maniura-Weber, S. F. Fucentese, A. Traweger, U. Silvan, J. G. Snedeker, *Biomaterials* **2020**, *249*, 120034.

[11] L. Li, R. Hao, J. Qin, J. Song, X. Chen, F. Rao, J. Zhai, Y. Zhao, L. Zhang, J. Xue, *Adv. Fiber Mater.* **2022**, *4*, 1375.

[12] K. Xi, Y. Gu, J. Tang, H. Chen, Y. Xu, L. Wu, F. Cai, L. Deng, H. Yang, Q. Shi, W. Cui, L. Chen, *Nat. Commun.* **2020**, *11*, 4504.

[13] G. Jiang, S. Li, K. Yu, B. He, J. Hong, T. Xu, J. Meng, C. Ye, Y. Chen, Z. Shi, G. Feng, W. Chen, S. Yan, Y. He, R. Yan, *Acta Biomater.* **2021**, *128*, 150.

[14] C. Puckert, E. Tomaskovic-Crook, S. Gambhir, G. G. Wallace, J. M. Crook, M. J. Higgins, *Acta Biomater.* **2020**, *106*, 156.

[15] X. Liu, M. Hao, Z. Chen, T. Zhang, J. Huang, J. Dai, Z. Zhang, *Biomaterials* **2021**, *272*, 120771.

[16] X. Liu, S. Song, Z. Chen, C. Gao, Y. Li, Y. Luo, J. Huang, Z. Zhang, *Acta Biomater.* **2022**, *151*, 148.

[17] M. Song, K. Martinowich, F. S. Lee, *Mol. Psychiatry* **2017**, *22*, 1370.

[18] O. J. Ziff, D. I. Bromage, D. M. Yellon, S. M. Davidson, *Cardiovasc. Res.* **2018**, *114*, 358.

[19] a) G. Courtine, M. V. Sofroniew, *Nat. Med.* **2019**, *25*, 898; b) B. Gong, X. Zhang, A. A. Zahrani, W. Gao, G. Ma, L. Zhang, J. Xue, *Exploration* **2022**, *2*, 20210035.

[20] N. Zhang, J. Lin, V. P. H. Lin, U. Milbreta, J. S. Chin, E. G. Y. Chew, M. M. Lian, J. N. Foo, K. Zhang, W. Wu, S. Y. Chew, *Adv. Sci.* **2021**, *8*, 2100805.

[21] a) E. Capuana, F. Lopresti, M. Ceraulo, V. La Carrubba, *Polymers* **2022**, *14*, 1153; b) M. F. P. Graça, S. P. Miguel, C. S. D. Cabral, I. J. Correia, *Carbohydr. Polym.* **2020**, *241*, 116364.

[22] a) K. Yue, G. Trujillo-de Santiago, M. M. Alvarez, A. Tamayol, N. Annabi, A. Khademhosseini, *Biomaterials* **2015**, *73*, 254; b) A. G. Kurian, R. K. Singh, K. D. Patel, J. H. Lee, H. W. Kim, *Bioact. Mater.* **2022**, *8*, 267; c) S. L. Ding, X. Liu, X. Y. Zhao, K. T. Wang, W. Xiong, Z. L. Gao, C. Y. Sun, M. X. Jia, C. Li, Q. Gu, M. Z. Zhang, *Bioact. Mater* **2022**, *17*, 81.

[23] V. R. Pattabiraman, J. W. Bode, *Nature* **2011**, *480*, 471.

[24] M. Jurak, A. E. Wiącek, A. Ładniak, K. Przykaza, K. Szafran, *Adv. Colloid Interface Sci.* **2021**, *294*, 102451.

[25] A. I. Aghmiuni, S. H. Keshel, F. Sefat, A. AkbarzadehKhiyavi, *Mater. Sci. Eng.: C* **2021**, *120*, 111752.

[26] a) L. Wang, Y. Qiu, Y. Guo, Y. Si, L. Liu, J. Cao, J. Yu, X. Li, Q. Zhang, B. Ding, *Nano Lett.* **2019**, *19*, 9112; b) X. Li, Y. Zhao, S. Cheng, S. Han,

M. Shu, B. Chen, X. Chen, F. Tang, N. Wang, Y. Tu, B. Wang, Z. Xiao, S. Zhang, J. Dai, *Biomaterials* **2017**, *137*, 73; c) Z. Chen, H. Zhang, C. Fan, Y. Zhuang, W. Yang, Y. Chen, H. Shen, Z. Xiao, Y. Zhao, X. Li, J. Dai, *ACS Nano* **2022**, *16*, 1986.

[27] a) T. Xin, Y. Gu, R. Cheng, J. Tang, Z. Sun, W. Cui, L. Chen, *ACS Appl. Mater. Interfaces* **2017**, *9*, 41168; b) C. Fan, W. Yang, L. Zhang, H. Cai, Y. Zhuang, Y. Chen, Y. Zhao, J. Dai, *Biomaterials* **2022**, *288*, 121689.

[28] B. Kaplan, U. Merdler, A. A. Szklanny, I. Redenski, S. Guo, Z. Bar-Mucha, N. Michael, S. Levenberg, *Biomaterials* **2020**, *251*, 120062.

[29] a) H. Liu, J. Zhang, X. Xu, S. Lu, D. Yang, C. Xie, M. Jia, W. Zhang, L. Jin, X. Wang, X. Shen, F. Li, W. Wang, X. Bao, S. Li, M. Zhu, W. Wang, Y. Wang, Z. Huang, H. Teng, *Theranostics* **2021**, *11*, 4187; b) S. Stern, B. J. Hilton, E. R. Burnside, S. Dupraz, E. E. Handley, J. M. Gonyer, C. Brakebusch, F. Bradke, *Neuron* **2021**, *109*, 3436.

[30] a) Y. Yang, Y. Lin, Z. Zhang, R. Xu, X. Yu, F. Deng, *Biomater. Sci.* **2021**, *9*, 3334; b) J. O. Abaricia, A. H. Shah, M. Chaubal, K. M. Hotchkiss, R. Olivares-Navarrete, *Biomaterials* **2020**, *243*, 119920; c) L. Lv, Y. Xie, K. Li, T. Hu, X. Lu, Y. Cao, X. Zheng, *Adv. Healthcare Mater.* **2018**, *7*, 1800675.

[31] a) F. Sun, J. Wang, Q. Sun, F. Li, H. Gao, L. Xu, J. Zhang, X. Sun, Y. Tian, Q. Zhao, H. Shen, K. Zhang, J. Liu, *J. Exp. Clin. Cancer Res.* **2019**, *38*, 449; b) A. N. Seneviratne, A. Edsfeldt, J. E. Cole, C. Kassiteridi, M. Swart, I. Park, P. Green, T. Khoyratty, D. Saliba, M. E. Goddard, S. N. Sansom, I. Goncalves, R. Krams, I. A. Udalova, C. Monaco, *Circulation* **2017**, *136*, 1140; c) B. H. Cha, S. R. Shin, J. Leijten, Y. C. Li, S. Singh, J. C. Liu, N. Annabi, R. Abdi, M. R. Dokmeci, N. E. Vrana, A. M. Ghaemmaghami, A. Khademhosseini, *Adv. Healthcare Mater.* **2017**, *6*, 1700289.

[32] R. Izmailyan, J. C. Hsao, C. S. Chung, C. H. Chen, P. W. Hsu, C. L. Liao, W. Chang, *J. Virol.* **2012**, *86*, 6677.

[33] a) K. Hu, B. R. Olsen, *J. Clin. Invest.* **2016**, *126*, 509; b) Y. Huang, B. He, L. Wang, B. Yuan, H. Shu, F. Zhang, L. Sun, *Stem Cell Res. Ther.* **2020**, *11*, 496.

[34] L. Gao, Z. Zhang, W. Xu, T. Li, G. Ying, B. Qin, J. Li, J. Zheng, T. Zhao, F. Yan, Y. Zhu, G. Chen, *Front. Mol. Neurosci.* **2019**, *12*, 42.

[35] Y. Rong, W. Liu, J. Wang, J. Fan, Y. Luo, L. Li, F. Kong, J. Chen, P. Tang, W. Cai, *Cell Death Dis.* **2019**, *10*, 340.

[36] M. Gao, Q. Dong, H. Yao, Y. Zhang, Y. Yang, Y. Dang, H. Zhang, Z. Yang, M. Xu, R. Xu, *Brain Behav. Immun.* **2017**, *59*, 288.

[37] E. J. Bradbury, E. R. Burnside, *Nat. Commun.* **2019**, *10*, 3879.

[38] H. S. Kwon, S. H. Koh, *Transl. Neurodegener.* **2020**, *9*, 42.

[39] Z. Álvarez, A. N. Kolberg-Edelbrock, I. R. Sasselli, J. A. Ortega, R. Qiu, Z. Syrgiannis, P. A. Mirau, F. Chen, S. M. Chin, S. Weigand, E. Kiskinis, S. I. Stupp, *Science* **2021**, *374*, 848.

[40] Z. Luo, W. Peng, Y. Xu, Y. Xie, Y. Liu, H. Lu, Y. Cao, J. Hu, *Acta Biomater.* **2021**, *136*, 519.

[41] A. Torres-Espín, J. Haefeli, R. Ehsanian, D. Torres, C. A. Almeida, J. R. Huie, A. Chou, D. Morozov, N. Sanderson, B. Dirlikov, C. G. Suen, J. L. Nielson, N. Kyritsis, D. D. Hemmerle, J. F. Talbott, G. T. Manley, S. S. Dhall, W. D. Whetstone, J. C. Bresnahan, M. S. Beattie, S. L. McKenna, J. Z. Pan, A. R. Ferguson, *eLife* **2021**, *10*, e68015.

[42] Y. Zhang, N. Sun, M. Zhu, Q. Qiu, P. Zhao, C. Zheng, Q. Bai, Q. Zeng, T. Lu, *Biomater. Adv.* **2022**, *133*, 112651.